NASA CONTRACTOR REPORT

NONLINEAR LIFT AND PRESSURE DISTRIBUTION OF SLENDER CONICAL BODIES WITH STRAKES AT LOW SPEEDS

by E. S. Levinsky and M. H. Y. Wei

Prepared by
AIR VEHICLE CORPORATION
La Jolla, Calif.
for Ames Research Center

NATIONAL AERONAUTICS AND SPACE ADMINISTRATION • WASHINGTON, D. C. • OCTOBER 1968

NASA CR-1202

NONLINEAR LIFT AND PRESSURE DISTRIBUTION OF SLENDER CONICAL BODIES WITH STRAKES AT LOW SPEEDS

By E. S. Levinsky and M. H. Y. Wei

Prepared under Contract No. NAS 2-3523 by
AIR VEHICLE CORPORATION
La Jolla, Calif.

for Ames Research Center

NATIONAL AERONAUTICS AND SPACE ADMINISTRATION

For sale by the Clearinghouse for Federal Scientific and Technical Information
Springfield, Virginia 22151 – CFSTI price $3.00

CONTENTS

NONLINEAR LIFT AND PRESSURE DISTRIBUTION OF SLENDER CONICAL BODIES WITH STRAKES AT LOW SPEEDS

By E. S. Levinsky and M. H. Y. Wei
Air Vehicle Corporation

SUMMARY

Nonlinear vortex lift and pressure distributions were obtained analytically for conical bodies of circular and elliptical cross-section with small span sharp-edged conical wings or strakes of arbitrary dihedral angle. The analytical approach, which is an extension of the Mangler and Smith theory for slender flat triangular wings, made use of a generalized conformal transformation to map this class of wing-bodies of high volumetric efficiency into a vertical slit. A single pair of spiral vortex sheets was assumed to originate from the leading edge of each strake. The shape and strength of the spiral vortex sheet were determined as part of the calculation procedure.

The nonlinear theory was evaluated by comparing with low-speed wind tunnel force and pressure data obtained on a series of related models. Both theory and experiment indicated relatively large increases in lift with even the smallest strake sizes considered, viz., 10% of the body radius. Good correlation between theory and experiment was obtained over the complete angle of attack range for cones with strakes of 50% of the body radius or greater. For these configurations, the lift was approximately twice the linear theory value at angles of attack α equal to twice the strake semi-apex angle δ. At $\alpha/\delta \simeq 6$, the lift was approximately four times the linear value.

For cones with 25% and 10% strakes, good correlation between theory and experiment was found except in the range $2 \leq \alpha/\delta \leq 4$. Both theory and experiment showed that the nonlinear lift was relatively small for $\alpha/\delta < 2$. For $2 < \alpha/\delta < 4$, the wind tunnel lift consistently exceeded the theory. The disagreement was believed caused by a second pair of body vortices not included in the theoretical model. For $\alpha/\delta > 4$, the theory became multivalued, with the extent of the multivalued α/δ region increasing with decreasing strake size and dihedral. Reasonable agreement between the data and the upper theoretical solutions was obtained, and again indicated large lift increases over the linear theory.

INTRODUCTION

The approach and horizontal landing of reentry vehicles and recoverable boosters of high volumetric efficiency are compromised by their low values of lift curve slope and lift/drag ratio. This has led to the consideration of deployable lift aids, e.g., paragliders, parachutes, rotors, etc. to improve the overall landing characteristics. The purpose of the present study is to calculate the improvement in lift that can be obtained by using small conical wings or strakes with sharp leading edges, which can be unfolded from a conical body at low speeds (fig. 1). The use of these strakes will increase the overall lift because of the increased planform area, and because the sharp leading edges will cause the flow to separate on the upper surface and form two or more spiral vortex systems which further increase the lift.

Considerable experimental and theoretical research has been carried out on the nonlinear vortex lift of low aspect ratio wings and slender bodies (refs. 1-12). Legendre (ref. 1) treated the problem of a flat triangular wing within the context of slender-body potential theory by assuming that the two spiral vortex sheets, which were shed from the leading edges, could be replaced by a pair of concentrated potential vortices. Legendre satisfied the Kutta condition at the leading edge, as well as the usual tangential flow boundary condition over the wing, but, as pointed out by Adams (ref. 2), failed to account properly for the forces on the feeding vortex sheet. Brown and Michael (ref. 3) subsequently introduced the zero total force condition on the potential vortices and feeding sheet, which they represented as a cut between the vortex and leading edge, and obtained an improved solution for the nonlinear lift. Bryson (ref. 4) extended the Brown and Michael type of analysis to slender bodies of revolution and treated both conical and cylindrical configurations. Schindel (ref. 5) extended Bryson's analysis to bodies of elliptical cross-section. In contrast to the analyses for flat wings with sharp leading edges, the theories for slender bodies required the additional specification of the location on the body at which the vortex sheet originates. This was done empirically. Pershing (ref. 6) considered the effect of secondary vortices for flat triangular wings. Squire (ref. 7) used the Brown and Michael model to analyze conically cambered wings. Jobe (ref. 8) treated zero thickness pointed wings of arbitrary camber and planform.

In comparing theory with experimental data (e.g., refs. 3 and 10), it was found that the Brown and Michael type theories (henceforth designated BM theories) gave the correct overall trend for the variation of lift with angle of attack and also provided a good estimate of the overall vortex strength. However, the BM theory was found to predict a vortex location which is too far outboard, and consequently significantly overpredicted the vortex lift. An improved theory which accounts for the distribution of vorticity in the spiral vortex sheet was therefore clearly called for.

This was supplied by Mangler and Smith (ref. 10), who again treated the flat triangular wing, but included a vortex sheet originating at the

leading edge and ending at a cut which connected to an isolated potential vortex. Mangler and Smith formulated the additional boundary conditions which must be satisfied along the sheet to determine its strength and location, viz., the continuity of pressure and normal velocity across the sheet. By including these additional sheet boundary conditions, an improved estimate of the nonlinear lift was obtained. In order to simplify the mathematics, Mangler and Smith assumed that the shape of the vortex sheet was a circular arc of approximately 160^{o} in the transformed plane, in which the trace of the wing is mapped into a vertical slit. The resulting values for overall lift were in much better agreement with test data, but the lateral positions of the isolated vortex were still found to be too far outboard, possibly because of the circular sheet constraint. This constraint was subsequently removed by Smith (ref. 11), who allowed the angular extent of the sheet to be arbitrary and its shape to be free. Smith broke up the sheet into a series of connecting straight line segments in the transformed plane. The first segment was connected to the wing leading edge, whereas the last segment was joined by a cut to the isolated potential vortex of unknown strength. Smith obtained the strength and position of the sheet segments and of the isolated vortex through a complicated iteration procedure, and found excellent agreement with test data for a sheet of 14 segments and of an angular extent of 157^{o} in the transformed plane.

An alternate approach by Sacks, et al., (ref. 12) for wings with curved or straight leading edges, replaces the spiral vortex sheet with a discrete vortex model. Their method is dependent upon a knowledge of the vortex shedding rate, which must be determined "semi-empirically" in order to obtain agreement with test results.

The current investigation extends the numerical procedure established by Smith to conical bodies of circular and elliptical cross-section with small-span triangular wings or strakes at arbitrary dihedral. A fundamental assumption is that only a single pair of leading edge vortex sheets need be considered, and that additional body vortices, if present, have a negligible effect on the overall lift. The basic difference between the current method and that of Smith is that a more general conformal transformation is used to map the wing-body cross-section into a vertical slit. To simplify the numerical work as much as possible, a minimal number of sheet segments (i.e., 6 segments) is used for a majority of the calculations. Because of the assumptions inherent in the nonlinear theory, a supporting wind tunnel test program was carried out by NASA investigators at the Ames Research Center.

In the following sections a review of the Mangler and Smith theory is first given, with emphasis on the modifications introduced by the more general configurations. Sample calculations are presented which include the effects of several geometric parameters. Finally, the theory is evaluated by comparing with recently obtained test results.

NOTATION

A	body cross-sectional area; also, a parameter
a	vertical half-dimension of elliptical body; also, radius of circular body
B	parameter
b	horizontal half-dimension of elliptical body
C_L	lift coefficient based on projected planform area
C_p	pressure coefficient
d_j	distance in the auxiliary plane from the isolated vortex to the j'th pivotal point of the vortex sheet
F	force in physical cross-flow plane
g	normalized vortex strength
i	$(-1)^{1/2}$
L	lift
ℓ	matrix [eq. (14)]
N	force normal to body axis
n	inward normal to vortex sheet (in physical cross-flow plane)
r	polar radius in physical plane
S	planform reference area, also conformal mapping plane
U	component (= V cos α) of stream velocity along x
V	free stream velocity
W	complex potential
x, y, z	Cartesian coordinates
Z	complex variable (= y + i z) in physical cross-flow plane
Z^*	complex variable (= y^* + i z^*) in auxiliary cross-flow plane

α	angle of attack
β	dihedral angle; also, vortex separation angle for cone only
Γ	vortex strength
$\gamma_{j-1/2}$	vortex strength/unit length along vortex sheet at intermediate point
δ	semi-apex angle of body-strake configuration, measured in the dihedral plane; also, differential operator
ϵ	a parameter defined by equation (9)
η	angle defined by equation (18)
η_o	a parameter defined by equation (A2)
θ_j	angle in auxiliary plane [= arg $(Z^*_j - Z^*_v)$]
λ	parameter [eq. (16)]; also, angle for minimum pressure
ξ_o	a parameter defined by equation (A2)
Φ	velocity potential
φ	angle between r and tangent to sheet
ϕ	defined by $\phi = \tan^{-1} \frac{B}{A}$
ρ	air density
σ	distance along vortex sheet, measured from leading edge of strake

Subscripts:

1	linear
2	nonlinear
c	cut
j	index
k	index
m	mean values
n	segment number

s	source
u	uncorrected
v	isolated vortex

Superscripts:

$\bar{}$	complex conjugate
*	in the auxiliary plane
(1), (2), (3)	index for initial values

THEORY

Consider the flow past a circular or elliptical conical body with sharp edged strakes with or without dihedral at angle of attack. It is assumed that a thin spiral vortex sheet emanates from each strake edge because of leading edge separation. No separation is assumed on the leeward body surface.

Using slender body theory, the two-dimensional Laplace equation holds in the physical cross-flow plane $Z\,(=y+iz)$ for the velocity potential Φ, i.e.,

$$\Phi_{yy} + \Phi_{zz} = 0 \tag{1}$$

The coordinate system used is shown in figure 2. To satisfy the usual tangential flow boundary condition on the body and strakes, it is convenient to solve the potential problem in an auxiliary plane $Z^* = Z^*(Z)$, in which the body and strakes are collapsed into a vertical slit along the y-axis (fig. 3). For the case of a flat plate delta wing, the transformation is

$$Z^{*2} = Z^2 - 1 \tag{2}$$

and was used by Mangler and Smith. For wing-body combinations of arbitrary dihedral angle β, the corresponding transformation, derived for the present study through use of an auxiliary S-plane (see fig. 4), is

$$Z^{*2} = \frac{1}{(b-a)^2}\left[b\left[Z^2 - (b^2 - a^2)\right]^{1/2} - aZ - i(b-a)\eta_o\right]^2 - \xi_o^2$$

The terms are explained in Appendix A.

Velocity Potential

Following Smith (ref. 11), the vortex sheet in the transformed Z^*-plane is represented by a series of n straight line segments of normalized

strength $g_j = -\left[\frac{d\Delta\Phi/d\theta}{U \tan \delta}\right]_{Z_j^*}$ at the pivotal sheet points Z_j^* (see fig. 3).

The j = 0 pivot is at the point that corresponds to the leading edge, i.e., $Z^* = 0$. The j = n pivotal point is joined through a cut to a potential vortex of normalized strength $g_v = \Gamma_v / U \tan \delta$ located at the point $Z_v^* = y_v^* + i\, z_v^*$.

The complex potential $W(Z^*)$ is then

$$\frac{W(Z^*)}{U \tan \delta} = -i \frac{\tan \alpha}{\tan \delta} Z^* - \frac{i g_v}{2\pi} \ln \left(\frac{Z^* - Z_v^*}{Z^* + \overline{Z}_v^*} \right)$$

$$- \frac{i}{4\pi} \sum_{j=1}^{n} g_j (\theta_{j+1} - \theta_{j-1}) \ln \left(\frac{Z^* - Z_j^*}{Z^* + \overline{Z}_j^*} \right) + \frac{W(Z^*)_s}{U \tan \delta} \qquad (3)$$

where θ_j is the angle between the line connecting Z_v^* and Z_j^*, and the line connecting Z_v^* with the origin (see fig. 3). Note that $\theta_o = 0$ and $\theta_{n+1} = \theta_n$. Equation (3) is identical with the corresponding expression of Smith (ref. 11), except for the addition of the source term $W(Z^*)_s$, caused by the expanding body cross-sectional area (see Appendix A). The first term on the right hand side gives the linear lift by slender body theory. The second term on the right hand side is the contribution from the two isolated vortices, and the summation represents the contribution from the vortex sheet segments.

The unknowns in equation (3) are g_v, Z_v^*, g_j, and Z_j^* with $j = 1, 2, \ldots n$. The total number of unknowns is 2n + 2, and therefore a like number of equations is required. The equations are supplied by the boundary conditions and the zero force condition, and are reviewed below.

Boundary Conditions

Kutta condition. —The Kutta condition states that a finite flow velocity must exist at the leading edge in the physical plane. In the Z^*-plane the Kutta condition becomes

$$\left[\frac{dW}{dZ^*} - \frac{dW_s}{dZ^*}\right]_{Z^* = 0} = 0$$

Differentiation of equation (3), and assuming that the terms in the summation vary linearly with θ between j = 0 and 1, give

$$g_v = 2\pi \frac{\tan\alpha}{\tan\delta}\left[2\frac{y_v^*}{y_v^{*2}+z_v^{*2}} + \left(\frac{g_1}{g_v}\right)\left(\frac{\theta_2^2}{\theta_2-\theta_1}\right)\frac{y_1^*}{y_1^{*2}+z_2^{*2}}\right.$$

$$\left. + \left(\frac{g_2}{g_v}\right)\left(\theta_3 - \frac{\theta_1\theta_2}{\theta_2-\theta_1}\right)\frac{y_2^*}{y_2^{*2}+z_2^{*2}} + \sum_{j=3}^{n}\left(\frac{g_j}{g_v}\right)\frac{\theta_{j+1}-\theta_{j-1}}{y_j^{*2}+z_j^{*2}}\,y_j^*\right]^{-1} \tag{4}$$

Equation (4) is formally identical with the flat wing result. The body and dihedral effects enter only through the transformation $Z^* = Z^*(Z)$.

Zero force condition. —The formulation of the zero force condition on the isolated vortex plus cut follows. The force F_v on the isolated vortex is

$$F_v = -i\rho\Gamma_v\Delta U \tag{5}$$

where ΔU is the local relative velocity between the flow and the vortex in the physical cross-flow plane, namely,

$$\Delta U = \lim_{Z\to Z_v}\left[\frac{d\overline{W}}{d\overline{Z}} + \frac{\Gamma_v}{2\pi i}\,\frac{1}{\overline{Z}-\overline{Z}_v}\right] - U Z_v \tan\delta \tag{6}$$

The force F_c on the cut may be written

$$F_c = i\rho U\Gamma_v (Z_v - Z_n)\tan\delta \tag{7}$$

Combining equations (5) - (7) with (3) gives for the conjugate of the total force

$$\overline{F}_v + \overline{F}_c = \lim_{Z\to Z_v} i\rho U\Gamma_v\tan\delta\left\{\overline{Z}_n - 2\overline{Z}_v + i\frac{dZ^*}{dZ}\left[\frac{g_v/2\pi}{Z^*+\overline{Z}^*} - \frac{\tan\alpha}{\tan\delta}\right.\right.$$

$$\left.\left. - \frac{1}{2\pi}\sum_{j=1}^{n}\frac{g_j(\theta_{j+1}-\theta_{j-1})\,y_j^*}{(Z_v^*-Z_j^*)(Z_v^*+\overline{Z}_j^*)} - \frac{g_v\epsilon}{2\pi} - \frac{iA}{\pi\tan\delta}\,\frac{dZ/dZ^*}{(Z^2-b^2+a^2)^{1/2}}\right]\right\} = 0 \tag{8}$$

where A is the local body cross-sectional area, and

$$\epsilon = \lim_{Z\to Z_v}\left[\frac{1}{Z^*-Z_v^*} - \frac{dZ/dZ^*}{Z-Z_v}\right]$$

The zero force condition as given by equation (8) depends on the body shape

through the transformation $Z^* = Z^*(Z)$ and through A. Note that ϵ, which represents the velocity contribution of the vortex itself in the transformed plane, less its velocity contribution in the physical plane multiplied by dZ/dZ^*, is nonsingular. Consecutive application of L'Hospital's rule gives

$$\epsilon = -\frac{1}{2}\frac{d^2Z/dZ^{*2}}{dZ/dZ^*} \tag{10}$$

which is also dependent upon body shape.

Pressure continuity condition.—The condition that the pressure is continuous across the vortex sheet has been shown in reference 10 to be

$$\Delta\Phi_{j-1/2} = \left\{\Delta\left(\frac{\partial\Phi}{\partial\sigma}\right)\left[r\cos\varphi - \left(\frac{\partial\Phi}{\partial\sigma}\right)_m / U\tan\delta\right]\right\}_{j-1/2} \tag{11}$$

where the Δ operator refers to the difference across the sheet at the midpoint of the j'th segment, $(\partial\Phi/\partial\sigma)_{m_{j-1/2}}$ is the mean velocity along the sheet at the midpoint of the j'th segment and is defined in the following section, and the remaining symbols are as shown in figure 2. Smith expresses the potential jump $\Delta\Phi_{j-1/2}$ in terms of the isolated vortex circulation Γ_v and the sheet strengths $\gamma_{j-1/2}$ at the intermediate points as

$$\Delta\Phi_{j-1/2} = \Gamma_v + \int_{\theta_{j-1/2}}^{\theta_n} (\gamma_{k-1/2})\, d\theta \tag{12}$$

where

$$\gamma_{k-1/2} = -\frac{(d\Delta\Phi/d\theta)_{k-1/2}}{U\tan\delta} \tag{13}$$

Using the trapezoidal rule for numerical integration, equation (12) may be written in matrix form as

$$\Delta\Phi_{j-1/2} = \Gamma_v + [\![\ell]\!]\,\{\!\{\gamma\}\!\} \tag{14}$$

The ℓ matrix is triangular, and for equal angular spacing between pivotal points ($\theta_j - \theta_{j-1} = \Delta\theta_j = \Delta\theta$) is of the form

$$\left[\!\left[\ell \right]\!\right] = \left[\!\left[\begin{matrix} \Delta\theta/2 & \Delta\theta & \Delta\theta & . & . & . \\ 0 & \Delta\theta/2 & \Delta\theta & . & . & . \\ 0 & 0 & . & & & \\ . & . & & . & & \\ . & . & & & . & \\ . & . & & & & . \end{matrix} \right]\!\right]$$

The γ matrix is a column matrix of n-j elements, with the k'th element evaluated at the midpoint of the k'th sheet segment according to equation (13).

The jump in tangential velocity $\Delta(\partial\Phi/\partial\sigma)_{j-1/2}$ at the intermediate points can be expressed in terms of the sheet strengths $\gamma_{j-1/2}$ through

$$\Delta(\partial\Phi/\partial\sigma)_{j-1/2} = U\tan\delta\left[\gamma\frac{d\theta}{d\sigma}\right]_{j-1/2} \tag{15}$$

Combining equations (11), (14), and (15) gives

$$g_v + \left[\!\left[\ell \right]\!\right] \left\{ \gamma \right\} = \left[\gamma_{j-1/2} \right] \left[\lambda_{j-1/2} \right] \qquad \text{with } j=1, 2, \ldots n \tag{16}$$

where

$$\lambda_{j-1/2} = -\left[d\theta/d\sigma \left[r\cos\varphi - (\partial\Phi/\partial\sigma)_m / U\tan\delta \right] \right]_{j-1/2}$$

Equations (16) form a set of n simultaneous equations in the n unknowns $\gamma_{j-1/2}/g_v$. The equations are actually nonlinear because the γ's, g_v, and the isolated vortex and midpoint coordinates appear in $\lambda_{j-1/2}$ in a complicated way. The g_j's are obtained from the $\gamma_{j-1/2}$'s by linear interpolation.

Continuity of normal velocity.— The continuity condition for the normal velocity across the sheet at the midpoint positions has been shown by Mangler and Smith to be

$$(\partial\Phi/\partial n)_{j-1/2} = -\left[r\,U\tan\delta\,\sin\varphi \right]_{j-1/2} \tag{17}$$

where $(\partial\Phi/\partial n)_{j-1/2}$ is the normal velocity at the midpoint of the j'th sheet segment. In order to satisfy equation (17), each sheet segment must be rotated through an angle $\eta_{j-1/2}$ (see fig. 3), where

$$\eta_{j-1/2} \simeq \left[\frac{r\,U\tan\delta\,\sin\varphi + \partial\Phi/\partial n}{(\partial\Phi/\partial\sigma)_m} \right]_{j-1/2} \tag{18}$$

and where it has been assumed that $\sin\eta_{j-1/2} \simeq \eta_{j-1/2}$ and $\cos\eta_{j-1/2} \simeq 1$.

The mean velocity along the sheet $(\partial\Phi/\partial\sigma)_{m_{j-1/2}}$ and normal velocity of the sheet $(\partial\Phi/\partial n)_{j-1/2}$ may be expressed in terms of coordinates in the

transformed plane. Thus, we have

$$(\partial \Phi/\partial \sigma)_{m_{j-1/2}} - i\,(\partial \Phi/\partial n)_{j-1/2} = \left[(dW/dZ^*)\ (dZ^*/d\sigma^*)\ (d\sigma^*/d\sigma)\right]_{j-1/2} \tag{19}$$

where σ^* is the arc length along the sheet in the transformed plane, i.e., $(d\sigma^*/d\sigma)_{j-1/2} = \left| dZ^*/dZ \right|_{j-1/2}$. The term $(dW/dZ^*)_{j-1/2}$ is obtained by differentiation of equation (3), and

$$\left[dZ^*/d\sigma^*\right]_{j-1/2} = \left[(dZ^*/d\theta)/(d\sigma^*/d\theta)\right]_{j-1/2}. \tag{20}$$

Both of the derivatives on the right hand side of the above equation may be evaluated from the coordinates of the vortex sheet in the transformed plane. Referring to figure 3, numerical evaluation yields

$$(dZ^*/d\theta)_{j-1/2} \simeq \left\{\frac{Z^*_{j-1/2} - (y^*_v + i z^*_v)}{d_{j-1/2}}\right\}\left[\frac{d_j - d_{j-1}}{\theta_j - \theta_{j-1}} + i d_{j-1/2}\right] \tag{21}$$

$$(d\sigma^*/d\theta)_{j-1/2} \simeq \left(d_j^2 + d_{j-1}^2\right)^{1/2} \tag{22}$$

The angle φ is defined in figure 1, and may be expressed in terms of the above quantities, viz.,

$$(\cos\varphi)_{j-1/2} = \left(\frac{dr}{d\sigma}\right)_{j-1/2} = \left[\left(\frac{dr}{d\theta}\right)\left(\frac{d\theta}{d\sigma^*}\right)\left(\frac{d\sigma^*}{d\sigma}\right)\right]_{j-1/2} \tag{23}$$

where

$$\left(\frac{dr}{d\theta}\right)_{j-1/2} \simeq \frac{r_j - r_{j-1}}{\theta_j - \theta_{j-1}}$$

After the $\eta_{j-1/2}$'s have been found from equations (18), the sheet shape must be changed by rotating each sheet segment through the angle $\eta_{j-1/2}$. This will change the polar distances d_j between the isolated vortex and the pivotal points. The new d_j's have been shown by Smith (ref. 11) to be

$$d'_j = d_j + \Delta d_j \tag{24}$$

with

$$\Delta d_j = \frac{d_j\,\Delta d_{j-1}}{d_{j-1}} - \frac{d_j^2 + d_{j-1}^2 - 2 d_j\, d_{j-1} \cos(\theta_j - \theta_{j-1})}{d_{j-1} \sin(\theta_j - \theta_{j-1})}\,\eta_j \tag{25}$$

Numerical Procedure

Equations (4), (8), (16), and (18) form the required set of $2n + 2$ equations, and were solved on the CDC 3600 computer at the University of California, San Diego by an iteration procedure.[1]

In brief, the numerical procedure was to linearize equations (16) by assuming an initial vortex sheet and isolated vortex (strengths and coordinates), and to insert these assumed values into the $\lambda_{i-1/2}$. Equations (16) and (4) were then solved for the sheet and isolated vortex strengths by iteration. Next, the position of the isolated vortex was adjusted until equation (8) was satisfied. An improved numerical procedure for accomplishing this is described below. Finally, the sheet shape was rotated according to equation (18), and the new transformed coordinates of the sheet were then found by applying equations (24) and (25). The entire procedure was repeated until convergence in sheet shape and strength was obtained.

Zero force condition iteration procedure.–Smith used the method of "steepest descent" as an iterative procedure to satisfy the force balance condition on the isolated vortex and cut. However, it was found that this method at best converges slowly, because the contours of constant unbalanced force are extremely eccentric, especially for the configurations with small strakes. The following iteration procedure due to Warner (ref. 13) was used instead, to obtain more rapid convergence.

According to this procedure, the net resultant force on the isolated vortex and cut was first written in terms of its y and z components,

$$\delta\vec{F} = \delta\vec{F}_v + \delta\vec{F}_c = \delta\vec{F}_y(y_v, z_v) + \delta\vec{F}_z(y_v, z_v) \tag{26}$$

where (y_v, z_v) is the assumed location of the isolated vortex, and in general $\delta\vec{F}_y \neq \delta\vec{F}_z \neq 0$. Next, denoting the values of the isolated vortex position which satisfy the zero force condition [equation (8)] by y_{v_o} and z_{v_o}, and assuming linearity,

$$\left\{\begin{aligned} y_v &= y_{v_o} + (\partial y_v/\partial F_y)\ \delta F_y + (\partial y_v/\partial F_z)\ \delta F_z \\ z_v &= z_{v_o} + (\partial z_v/\partial F_y)\ \delta F_y + (\partial z_v/\partial F_z)\ \delta F_z . \end{aligned}\right\} \tag{27}$$

By taking three different initial values $(y_v, z_v)^{(k)}_{k=1,2,3}$ we obtain in matrix form:

---

[1] The FORTRAN IV program has been delivered to Ames Research Center and checked out on the Center's IBM 7094/7040 Direct-Coupled System.

$$\begin{bmatrix} \delta F_y^{(1)} & \delta F_z^{(1)} & 1 \\ \delta F_y^{(2)} & \delta F_z^{(2)} & 1 \\ \delta F_y^{(3)} & \delta F_z^{(3)} & 1 \end{bmatrix} \begin{bmatrix} \partial y_v / \partial F_y & \partial z_v / \partial F_y \\ \partial y_v / \partial F_z & \partial z_v / \partial F_z \\ y_{v_o} & z_{v_o} \end{bmatrix} = \begin{bmatrix} y_v^{(1)} & z_v^{(1)} \\ y_v^{(2)} & z_v^{(2)} \\ y_v^{(3)} & z_v^{(3)} \end{bmatrix} \tag{28}$$

which represents six equations for the six unknowns in the second matrix. Only the two unknowns y_{v_o} and z_{v_o} need be obtained. The computed values of y_{v_o} and z_{v_o} are denoted as $y_v^{(4)}$ and $z_v^{(4)}$ from which $\delta F_y^{(4)}$ and $\delta F_z^{(4)}$ are subsequently obtained. Then the poorest previous approximation, measured by a quantity like $\left[\delta F_y^2 + \delta F_z^2 \right]$, is replaced by the values of superscript four. This process is repeated until the error formed by $\left[\delta F_y^{(4)^2} + \delta F_z^{(4)^2} \right]$ becomes smaller than the prescribed tolerance.

Initial trial solution.—Each calculation required a trial solution, "guess", from which the iteration procedure was initiated. The iteration procedure was found to fail if the initial guess was not reasonably close to the final solution. In order to minimize running time on the CDC 3600 computer, the final output from one calculation was automatically inserted as an initial guess for a subsequent calculation. It was thereby possible to make a set of calculations for either a single configuration at progressively increasing or decreasing values of angles of attack, or a progressively changing configuration at a fixed angle of attack, with only a single initial guess.

Lift and Pressure Distribution

Both the lift and local pressure distribution may be readily calculated once the solution for the vortex sheet has been found. The normal force N is obtained by computing the flow of downward momentum through an infinite plane normal to the body axis at the trailing edge, and is

$$N = - \rho U \int \int \left[\frac{\partial \Phi}{\partial z} - U \tan \alpha \right] dy \, dz \tag{29}$$

Taking $L = N \cos \alpha$ and using Green's theorem, this reduces to

$$L = - \rho U \cos \alpha \oint \Phi \, dy - \rho A U^2 \sin \alpha \tag{30}$$

where A is the body cross-sectional area, and the integration is carried out along a closed contour surrounding the body and vortex sheet. It is

convenient to write L in terms of the complex potential W as evaluated in the Z^*-plane,

$$L = - \mathrm{Re}\left[\rho U \cos\alpha \oint W \frac{dZ}{dZ^*}\, dZ^*\right] - \rho A U^2 \sin\alpha \qquad (31)$$

By the theory of complex functions, the radius of integration may be extended to infinity. The complex potential W is given by equation (3), with the sheet and isolated vortex coordinates and strengths assumed known. The source term in W gives no direct contribution to the lift.

For convenience, the lift will be divided into the linear lift L_1, and the nonlinear lift L_2 due to the isolated vortex and sheet. The linear lift is

$$L_1 = \mathrm{Re} \oint i\left[\rho U^2 (\sin\alpha)\, Z^* \frac{dZ}{dZ^*}\right] dZ^* - \rho A U^2 \sin\alpha$$

Going to the infinite circle, and using the wing-body transformation given in Appendix A, we have

$$\lim_{Z^* \to \infty} \frac{dZ}{dZ^*} = 1 - \frac{1}{2}\left[\frac{\xi_o^2 + b\,(b+a)}{Z^{*2}}\right] + 0\left[\frac{1}{Z^{*4}}\right]$$

Applying the theory of residues,

$$L_1 = \pi \rho U^2 \left[\xi_o^2 + b^2\right] \sin\alpha \qquad (32)$$

Equation (32) gives the linear lift for conical wing-bodies of circular or elliptical cross-section of width 2b and of overall length $x = 1/\tan\delta$. The quantity ξ_o is dependent upon the wing dihedral angle and relative body dimensions [equation (A2) of Appendix A]. For circular bodies with zero dihedral, Eq. (32) reduces to the well-known theory by Spreiter (NACA TR 962).

In terms of lift coefficient based on the projected planform area and free stream dynamic pressure ($C_{L_1} = 2 L_1 / \rho V^2 x \cos\beta$), we obtain

$$\frac{C_{L_1}}{\cos^2\alpha \tan^2\delta} = 2\pi \left[\frac{\sin\alpha}{\tan\delta}\right]\left[\xi_o^2 + b^2\right] \frac{1}{\cos\beta} \qquad (33)$$

For the nonlinear lift, we expand the logarithmic terms in equation (3), which arise from the isolated vortex and vortex sheet, for large Z^*. Similarly, by the theory of residues, we obtain

$$\frac{C_{L_2}}{\cos^2\alpha \tan^2\delta} = 2\left[g_v(Z_v^* + \bar{Z}_v^*)\cos\alpha + \frac{1}{2}\sum_{j=1}^{n} g_j(\theta_{j+1} - \theta_{j-1})(Z_j^* + \bar{Z}_j^*)\cos\alpha\right]\cos^{-1}\beta \tag{34}$$

According to slender body theory the local pressure coefficient C_p is approximated by

$$C_p = \sin^2\alpha - 2\frac{\Phi_x}{U}\cos^2\alpha - \frac{\Phi_y^2 + \Phi_z^2}{U^2}\cos^2\alpha \tag{35}$$

where in terms of the complex potential $W(Z^*)$

$$\Phi_y^2 + \Phi_z^2 = \left[\frac{dW}{dZ^*}\right]\left[\frac{d\bar{W}}{d\bar{Z}^*}\right]\left[\frac{dZ^*}{dZ}\right]\left[\frac{d\bar{Z}^*}{d\bar{Z}}\right] \tag{36}$$

The condition of conical flow requires

$$\Phi_x/\tan\delta = \mathrm{Re}(W) - y\,\mathrm{Re}\left[\frac{dW}{dZ^*}\frac{dZ^*}{dZ}\right] - z\,\mathrm{Im}\left[\frac{dW}{dZ^*}\frac{dZ^*}{dZ}\right] \tag{37}$$

It is noted that the ratios $\sin\alpha/\tan\delta$ and $\tan\alpha/\tan\delta$ occur implicitly in equations (33) through (37). For simplicity both parameters were assumed identical in the sample calculations to be discussed, and were referred to as α/δ. This is a valid approximation up to α approaching 20°. In comparing with the experimental data, the parameter $\sin\alpha/\tan\delta$ was used.

Sample Calculations

A number of computations were made on the CDC 3600 computer by the above procedure. The majority of calculations employed a six-segment vortex sheet model, which was found to give a satisfactory prediction of the total lift and isolated vortex position (table I), and yet did not consume an unreasonable amount of machine time, viz., approximately 10 seconds for each angle of attack. The computations were performed for the body-strake configurations listed in table II. The parameters investigated included the effects of body shape (body height to width ratio a/b), strake dihedral angle β, and strake size upon the overall lift coefficient $C_L/\cos^2\alpha\tan^2\delta$ and upon the position of the isolated vortex. Typical results are presented in figures 5-7. Additional results may be found in reference 14.

As expected, significant increases in lift beyond linear theory values were calculated. Figure 5(a) shows the variation in lift with α/δ for a family of elliptical cones with cross-sections ranging from circular (a/b = 1)

to a flat plate (a/b = 0), all with zero dihedral strakes of exposed semispan equal to 50% of the semi major cone axis (50% strakes). The results, which are typical of all calculations made for cones with large strakes (50% or greater), show an overall lift approximately twice the linear theory value at $\alpha/\delta \simeq 2$, and approximately four times the linear value at $\alpha/\delta \simeq 6$. As shown, the effect of body volume (a/b) was relatively small.

The y and z coordinates of the isolated vortex are shown in figure 5(b). As anticipated, the isolated vortex is shown to move upward and inboard from the strake tips with increasing incidence angle. A tendency for the isolated vortex to turn outboard with increasing α/δ was found at the larger α/δ. However, the accuracy in the calculation of vortex position is reduced at the higher α/δ, because the contours y_v versus z_v for a fixed value of the residual force on the vortex and cut become increasingly elongated in this region.

Figures 6 and 7 show the effect of strake dihedral for circular bodies with 25% and 10% strakes, respectively. The lift at large α/δ was found to increase progressively with decreasing dihedral angle in the range $+10^{\circ} \leq \beta \leq -20^{\circ}$, the configurations with largest negative dihedral showing the largest lift (figs. 6 and 7). Conversely, at low α/δ a small favorable effect of dihedral on lift was calculated. Similar trends were also calculated for cones with 50% and larger strakes.

The isolated vortex positions shown in figures 6 and 7 indicate that positive dihedral tends to move the vortex position inboard, whereas negative dihedral moves it outboard at all except the very lowest angles of attack. This larger outboard vortex displacement could account for the increased lift with negative dihedral angle.

At intermediate α/δ the lift is seen to be multivalued, with the extent of the multivalued region being greatest for the cones with the smallest strakes at the most negative dihedral angles. In the multivalued region the theoretical lift has three different values at a given α/δ corresponding to three distinct theoretical solutions. The lowest value corresponds to a solution with a weak vortex sheet lying close to the strake leading edge, the highest value is a solution with a strong vortex sheet with the isolated vortex located approximately one body radius above the strake, and the middle (transitional) value corresponds to a solution of intermediate nature.

Special calculation procedures were required to obtain the three different values. The usual calculation procedure was to begin with a trial solution at $\alpha/\delta \simeq 8.0$, and to obtain the entire lift curve by successively decreasing α/δ, using the previous solution as an initial trial for the next α/δ. In this manner, solutions were found automatically down to $\alpha/\delta \simeq 0.3$, as long as the lift was not multivalued. If the lift was multivalued, the standard procedure failed when α/δ was decreased below the region for the upper values. In order to obtain the lower values, it was necessary to begin with an initial trial solution at a low α/δ, say $\alpha/\delta \simeq 0.30$, and then successively increase α/δ. A transitional value was found by iterating upon a trial

solution at an intermediate α/δ as obtained from a single-valued solution for a larger strake size. The transitional curve was then generated by successively changing α/δ. Only a limited number of calculations were made for the lower and transitional values, because of the more complicated computation procedure required.

As a further check on the nature of the multivalued solutions, calculations were also made by the simplified Brown and Michael (BM) method mentioned previously in the Introduction. The BM theory was extended to include more general wing-body configurations, as outlined in Appendix B. It is noted that the independent parameter of the BM theory is taken as the vertical position of the isolated vortex above the body axis z_v, and not α/δ. The lift from the extended BM theory was found to be single-valued for large strake sizes, and multivalued for the smaller strakes, and generally followed the same trends as the extended Mangler and Smith calculations. Because of the relatively simple nature of the calculations, all three values of the lift curve were readily obtained (figure 8).

It is recognized that the prediction of a multivalued lift curve may well be the result of several simplifying assumptions in the theory, e.g., the neglect of a possible second pair of vortex sheets caused by boundary layer separation on the body and the neglect of regions of trapped flow, such as at the strake-cone junction. The requirement for an experimental verification of the theory is thereby increased. A comparison between the results of a test program and the theory is given in the following sections, including an assessment of the physical significance of the multivalued lift solutions.

WIND TUNNEL TESTS

A supporting wind tunnel program was carried out by NASA investigators in the 7 x 10 ft. low speed wind tunnel at the Ames Research Center to provide test results for evaluating the nonlinear lift theory.

Model Geometry

The models consisted of a series of circular and elliptical cones, each of 4-foot length. The circular cones were of semi-apex angles 2^o, 4^o, 6^o, 8^o, and 10^o. Each cone could be fitted with a series of strakes with exposed semispans of 10%, 25%, 50%, 75%, and 100% of the body radius. The 4^o circular cone and the corresponding 10%, 25%, and 75% strakes were instrumented for static pressures at a number of different axial stations (see fig. 9). The two elliptical cones were of 10^o maximum semi-apex angle and could be fitted with the same strakes as the 10^o circular cone. The ratios of the minor to major axes for the elliptical cones were $a/b = 0.6$ and 0.75. The elliptical cone-strake model with $a/b = 0.6$ is shown installed on the support strut in figure 10.

Test Procedure and Conditions

The angle of attack of the models was varied from -8° to approximately 34° for the majority of the force runs, and from -34° to 34° for the majority of the pressure tests. The force tests were initially carried out by pitching the model in the vertical plane. However, because of abnormally large tares believed caused by strut interference, the models were subsequently rolled 90° on the sting mount and pitched in the horizontal plane. An 8-inch sting extension was also added to further reduce strut interference. The pressure tests were pitched in the horizontal plane with the extension installed. The tests were conducted at nominal free-stream dynamic pressures of 50 and 75 psf, although some runs with the smaller strakes were made at dynamic pressures as high as 100 psf.

Data Reduction and Corrections

Six component force and moment data were measured with a mechanical scale system. Only the lift force data are presented for comparison with theory. The pressure data were obtained by scaling manometer board photographs. All coefficients are based upon the planform reference area $S = 16 \tan \delta \text{ ft}^2$, where δ is the strake semi-apex angle.

No wind tunnel wall corrections were made to the data. Because of the large buoyancy correction found in pitch, most of the force data in pitch were rerun in yaw. The remaining pitch data were corrected as follows:

$$C_L = C_{L_u} - \left(C_{L_u}\right)_{(\alpha=0)} (1 - \alpha/24) \qquad \alpha \le 24^{\circ}$$

$$C_L = C_{L_u} \qquad \alpha \ge 24^{\circ}$$

$$\alpha = \alpha_u$$

The above tare was obtained by comparing data from tests in the vertical and horizontal planes for several identical models, and was most pronounced for models of smallest span. The correction was not believed adequate for the cone of 2° semi-apex angle, and these data are therefore omitted.

EVALUATION OF THE THEORY

A theory has been developed for the pressure distribution and nonlinear lift of slender conical bodies with sharp leading edge strakes. Among the principal assumptions in the theory are (1) the representation of the complete leading edge spiral vortex sheet by a segmented feeding sheet of approximately 1/2 turn, together with an isolated potential vortex at the center; (2) the neglect of possible additional vortices caused by boundary layer

separation; (3) the neglect of regions of trapped flow, such as at the strake-body junction; and, (4) the neglect of vortex breakdown and other nonconical effects.

Comparisons of the theory with the wind tunnel lift and pressure data and an evaluation of the theoretical model follow.

Force Data

Circular cones.—Comparisons of the experimental and theoretical lift are presented in figures 11-16 for circular cones with strakes of exposed semispan equal to 0%, 10%, 25%, 50%, 75%, and 100% of the body radius, respectively. The wind tunnel data are for circular cone bodies with semi-apex angles δ of 4°, 6°, 8°, and 10°. The data for different apex angles are normalized in terms of the theoretical lift and angle of attack parameters $C_L/\tan^2\delta \cos^2\alpha$ and $\sin\alpha/\tan\delta$, respectively.

Excellent agreement between theory and experiment was found for strakes of exposed semispan equal to 50% of the body radius or larger over nearly the entire experimental angle of attack range (figs. 13 - 16). Some tendency for the data to drop below the theory is noted at the highest value of $\sin\alpha/\tan\delta$ for each model, and is attributed to the occurrence of vortex breakdown.

The comparison of the cone only data with the nonlinear theory is given in figure 11. In this case, the separation point on the model is no longer fixed by a strake. The nonlinear theory was applied by setting $a = 1$ (zero strake) and allowing the separation angle β to vary parametrically. A spiral vortex sheet was calculated emanating from the cone at the indicated separation angles. As seen in figure 11, β apparently decreases with increasing $\sin\alpha/\tan\delta$. This is in accordance with flow visualization observations by previous investigators (ref. 15). It is also apparent from figure 11 that the body vortices have a negligible influence on the overall lift when $\sin\alpha/\tan\delta < 2$, irrespective of the actual value of β. This is in agreement with the previous simplified theory for cones by Bryson (ref. 4) which does not include the effect of a feeding vortex sheet.

Both the 10% and 25% strake data, figures 12 and 13, show good agreement with the nonlinear theory up to $\sin\alpha/\tan\delta \simeq 2$ to 2.5. In the range $2.5 < \sin\alpha/\tan\delta < 4$ the wind tunnel data consistently exceed the theoretical lift. Beyond $\sin\alpha/\tan\delta = 4$ the theory becomes multivalued, and the wind tunnel data follow the upper theoretical curve. It is apparent that the data smoothly join the so-called upper and lower branch curves of the theory, and that the transition is gradual rather than abrupt. No experimental evidence for multiple lift values was found.

It appears that these anomalies can be explained by the possible existence of a second pair of body vortices (figure 17). Examination of the theoretical pressure distributions on the body shows a region of adverse pressure gradient and resulting possible flow separation on the leeward surface at low

to intermediate $\sin \alpha / \tan \delta$. The extent of this region is shown in figure 18 for cones with 10%, 25%, and 75% strakes. It is noted that the adverse region decreases rapidly with increasing strake size. For those theoretical solutions which are multivalued over a particular $\sin \alpha / \tan \delta$ range, the adverse region is shown to be largest on the lower curve and nonexistent along the upper branch curve. Thus when $C_L / \tan^2 \delta \cos^2 \alpha$ is multivalued, the upper branch solution is physically acceptable in that no separation and accompanying formation of body vortices are predicted. The lower and middle branch curves are physically unacceptable, because these solutions would lead to the formation of additional body vortices which are not included in the assumed flow model. It is therefore expected that the data should agree much better with the upper branch curve.

Below the multivalued region (i.e., $\sin \alpha / \tan \delta \lesssim 4$), the lower branch curves for small strake sizes should be corrected for the influence of the body vortices. As discussed previously in connection with the cone only results in figure 11, the body vortices are very weak and have only a negligible effect on lift for $\sin \alpha / \tan \delta \lesssim 2$. That this is true for cones with small strakes as well may be seen from the close correlation between the theory and data for $\sin \alpha / \tan \delta \lesssim 2$ in figures 12 and 13. Thus, as summarized in figure 17, the body vortices play a significant role only when $2 \lesssim \sin \alpha / \tan \delta \lesssim 4$.

In lieu of a complete theory, an approximate treatment to explore the relative magnitude of the effects of body vortices was attempted. The theoretical body vortex lift increments for the cone, with $\beta = 40^\circ$, were added to the lower branch solutions. The results, shown in figures 12 and 13, are encouraging. It appears that the proper flow model for bodies with small strakes should allow for the simultaneous formation of body vortices as well as strake vortices in this intermediate angle of attack range. The strength and position of these vortices and their feeding sheets could be found by simultaneously satisfying the proper boundary conditions across the vortex sheets as was done for the leading edge vortices. However, any such theory would be dependent upon knowledge of the body separation point, which must be found experimentally. Until such data are available, the approximation by super position can be considered.

It is of practical interest that the addition to the cone of even the smaller 10% and 25% strakes produced relatively large increases in lift at $\sin \alpha / \tan \delta \gtrsim 2$, as summarized in figure 19. The relative lift increase due to strakes is even larger than the percent gain shown in the parameter $C_L / \cos^2 \alpha \tan^2 \delta$ because of the larger planform area and semi-apex angle δ with strakes. Based on these results, the use of small deployable strakes in order to achieve additional lift and control on recoverable booster or spacecraft configurations appears to warrant consideration.

Elliptical cone.—A similar comparison between theory and experiment for the elliptical cone ($a/b = 0.6$) with 10%, 25%, and 50% strakes is given in figures 20-22, respectively. Good agreement is found for the 25% and 50% strake configurations at all values of $\sin \alpha / \tan \delta$, whereas the 10% strake data

exceed the theoretical lift at intermediate $\sin\alpha/\tan\delta$. The data for the $a/b = 0.75$ cone showed similar trends, with the role of the body vortices tending to diminish with decreasing a/b.

Lift data for the $a/b = 0.6$ cone without strakes are compared with the strake-on data in figure 23, and again show a sizable favorable effect with even the smallest strakes.

Pressure Data

Pressure data were obtained on a single circular cone of semi-apex angle 4°. The strake sizes tested were of exposed semispan equal to 10%, 25%, and 75% of the body radius. Measurements were made at a number of different axial stations. The axial variation of pressure coefficient at a constant percent span was generally typical of that presented in figure 24 and showed significant nonconical effects near the base. The data at the 63% station were compared with theory, since this position afforded a compromise between the adverse nonconical effects due to the base and the relatively thick boundary layer and the limited number of pressure orifices at more forward locations.

Although the upper surface pressure orifices were located primarily on the port side and the lower orifices primarily on the starboard side of the model, complete spanwise coverage with 10% and 25% strakes was obtained by testing at positive and negative incidence. The data scatter are believed due to flow and model asymmetries and to runs at different dynamic pressure.

A comparison between experimental and theoretical pressures for the circular cone without strakes is given in figure 25. The theory without strakes was based on a body separation angle β which varied with $\sin\alpha/\tan\delta$, and gave the best fit with the force data. Also shown on figure 25 are previously published data for a $\pm 0^\circ$ semi-apex angle cone (ref. 16). The asymmetries in the data from reference 16 were attributed to small irregularities in the model, and increased with increasing angle of attack.

The spanwise pressure data for a cone with 10% strakes are presented in figure 26. At $\sin\alpha/\tan\delta = 1.81$, reasonable correspondence with the nonlinear theory is indicated. At $\sin\alpha/\tan\delta = 3.14$, the data show significantly lower pressures on the upper cone surface, as might be expected from the presence of additional body vortices. The pressures on the lower surface agree well with theory for these cases. At $\sin\alpha/\tan\delta = 5.29$, the theory is based on the upper branch solution. The large scatter in the pressure data on the upper body surface makes comparison with theory difficult for this condition. It was observed that high negative pressure peaks appeared on either the upper right or left side of the model at this condition. Repeat runs showed apparently random changes of this phenomena from left to right sides. The cause of these loading asymmetries is now believed due to model irregularities smaller than usually considered acceptable. Nose blunting, as must be incorporated on a practical vehicle, or a small keel, as used in reference 16, should alleviate this problem.

Typical 25% strake data are shown in figure 27. The comparison with theory is somewhat similar to that for the 10% strakes in that good correlation is found at $\sin\alpha/\tan\delta = 1.59$, whereas pressures well below the theoretical values are found on the upper body surface for $\sin\alpha/\tan\delta = 3.15$. Excellent agreement is found on the lower surfaces for these cases. Asymmetries at $\sin\alpha/\tan\delta = 5.37$ again compromise the comparison with theory at large α.

The 75% strake pressure data are summarized in figure 28. Excellent agreement with theory is found for $\sin\alpha/\tan\delta = 1.7$. The data for $\sin\alpha/\tan\delta = 2.8$ and 3.8 show a good correlation with theory on the lower surfaces and also on the upper body surface, an indication that no body vortices are present. Pressures well below the theory were measured on the upper strake surfaces at $\sin\alpha/\tan\delta = 2.8$ and 3.8. A similar disagreement was found by Smith (ref. 11) and Hummel (ref. 17) for flat delta wings and was attributed to boundary layer separation with the formation of secondary and tertiary vortices near the wing tips.

CONCLUSIONS

A nonlinear theory has been developed for the lift and pressure distribution on conical body-strake configurations. The theory was evaluated by comparing with wind tunnel force and pressure data. The following results are noted:

(1) Both theory and experiment show that very large increases in lift may be obtained at a given angle of attack, even with the smallest strake size considered, viz., 10% of the body radius.

(2) Good correlation between theory and experiment was obtained for lift over the complete angle of attack range, except for the 10% and 25% strake configurations in the range $2 \leq \sin\alpha/\tan\delta \leq 4$. The nonagreement for these cases is believed caused by a second pair of spiral vortex sheets which originate on the upper body surface, and which are not included in the theoretical model.

(3) Improvement of the theory to account for the body vortices requires additional experimental verification of their formation and determination of the body separation point.

Air Vehicle Corporation
La Jolla, California
February 6, 1968

APPENDIX A

GENERALIZED CONFORMAL TRANSFORMATIONS

The transformation

$$Z^{*2} = \frac{1}{(b-a)^2}\left[b\left(Z^2 - (b^2 - a^2)\right)^{1/2} - aZ - i(b-a)\,\eta_o\right]^2 - \xi_o^2 \tag{A 1}$$

maps the contour of strake-body combinations of circular or elliptical body cross-section in the physical Z-plane into a vertical slit along the imaginary axis in the auxiliary Z^*-plane (figs. 3 and 4). Here ξ_o and η_o are defined as

$$\left.\begin{aligned} \xi_o &= \frac{1}{b-a}\left[b\left(A^2 + B^2\right)^{1/4} \cos\frac{\phi}{2} - a\cos\beta\right] \\ \eta_o &= \frac{1}{b-a}\left[b\left(A^2 + B^2\right)^{1/4} \sin\frac{\phi}{2} - a\sin\beta\right] \end{aligned}\right\} \tag{A 2}$$

with

$$A = \cos 2\beta - (b^2 - a^2), \quad B = \sin 2\beta, \quad \text{and } \phi = \tan^{-1}\frac{B}{A},$$

where a is the radius of minor body axis, b is the radius of major body axis, and β is the angle between the line joining the strake tip with the body axis and the y axis. It is noted that the strakes in the physical Z-plane are slightly curved, as shown in figure 4, and that the y distance between strake tips is $2\cos\beta$.

By expanding equation (A 1) in terms of b-a and taking the limit $(b-a)\to 0$, it can readily be seen that equation (A 1) reduces to the corresponding transformation for circular cross-sections, which is

$$Z^{*2} = \left[(Z - a^2/Z) - i\,\eta_o\right]^2 - \xi_o^2 \tag{A 3}$$

with

$$\xi_o = (1 - a^2)\cos\beta, \quad \eta_o = (1 + a^2)\sin\beta.$$

Taking $a = 1$ gives a circular cone with vanishingly small strakes at arbitrary β. Taking $a = \beta = 0$ gives a flat triangular wing with no body.

The source term for elliptical cross-sections is derived by applying equation (A 1) to a well-known source term for circular cross-sections, and is

$$\frac{dW_s/dZ}{U \tan \delta} = \frac{a\,b}{[Z^2 - (b^2 - a^2)]^{1/2}} \qquad (A\,4)$$

APPENDIX B

BROWN AND MICHAEL THEORY

The simplified Brown and Michael model, in which the coiled vortex sheet and isolated vortex are replaced by a single pair of concentrated vortices, is a limiting case of the MS theory when n = 0. In the present paper use is made of the BM limit to investigate the general variation of lift coefficient as a function of angle of attack, primarily for configurations with small strakes, for which some difficulty was encountered in the MS approach. It is recognized, as indicated in the Introduction, that the lift values and lateral vortex position obtained from the BM theory are too large. Nevertheless, these simple calculations serve as a guide for establishing the overall shape of the C_L vs. α curve when the number of MS calculations is insufficient. A brief review of the BM theory follows.

The BM formulation is similar to the MS theory already discussed, except that it is no longer necessary to satisfy boundary conditions on the sheet. What remains is to solve the two-dimensional Laplace equation in the cross-flow plane subject to the boundary conditions of zero normal velocity on the surface of the body and strakes, the Kutta condition at the tips of the strakes, and the force balance condition on the vortex and cut.

Equation (3) for the complex potential in the Z^*-plane now reduces to

$$W = U \alpha Z^* - \frac{i \Gamma_v}{2\pi} \ln \left(\frac{Z^* - Z_v^*}{Z^* + \overline{Z}_v^*} \right) + W_s(Z^*) \qquad \text{(B 1)}$$

which has two unknowns, the position of the isolated vortex Z_v^* and its strength Γ_v. They may be determined from the Kutta condition and the zero force condition which are, respectively,

$$\frac{2\pi}{g_v} \left(\frac{\alpha}{\tan \delta} \right) = \frac{1}{Z_v^*} + \frac{1}{\overline{Z}_v^*} \qquad \text{(B 2)}$$

and

$$\overline{Z}_t - 2\overline{Z}_v = \left(\frac{g_v}{2\pi i} \right) \frac{dZ^*}{dZ} \left[\frac{1}{Z^* + \overline{Z}_v^*} - \epsilon \right] + i \frac{dZ^*}{dZ} \left(\frac{\alpha}{\tan \delta} \right) - \frac{dW_s/dZ}{U \tan \delta} \qquad \text{(B 3)}$$

where $\overline{Z}_t$ is the conjugate of the Z coordinate of the strake tip.

The procedure that was followed was to eliminate $\alpha/\tan\delta$ between equations (B 2) and (B 3) and gave the following expression for g_v.

$$\frac{g_v}{2\pi i} = \left\{ \frac{\dfrac{dW_s/dZ}{U \tan\delta} - 2\,\overline{Z}_v + \overline{Z}_t}{\dfrac{Z_v^* + \overline{Z}_v^*}{Z_v^* \cdot \overline{Z}_v^*} + \epsilon - \dfrac{1}{Z_v^* + \overline{Z}_v^*}} \right\} \left(\frac{dZ}{dZ^*}\right)_v \tag{B 4}$$

Equation (B 4) was solved by fixing the z coordinate of the vortex, and varying the y coordinate until g_v became real. This was carried out on the CDC-3600 computer in complex arithmetic. After g_v was obtained, the corresponding $\alpha/\tan\delta$ was computed from equation (B 2).

ACKNOWLEDGMENT

The authors gratefully acknowledge their indebtedness to Mrs. Claudia B. Lowenstein, without whose programming skill and exceptional dedication this report could not have been written.

REFERENCES

1. Legendre, R.: Écoulement au voisinage de la pointe avant d'une aile à forte flèche aux incidences moyennes. La Recherche Aéronautique (O.N.E.R.A.), No. 30, Nov.-Dec. 1952, pp. 3-8; No. 31, Jan.-Feb. 1953, pp. 3-6.

2. Adams, Mac C.: Leading-Edge Separation From Delta Wings at Supersonic Speeds. Journal of the Aeronautical Sciences (Readers' Forum), Vol. 20, No. 6, June 1953, p. 430.

3. Brown, C. E., and Michael, W. H., Jr.: On Slender Delta Wings with Leading Edge Separation. NACA TN 3430, April 1955. Also: Journal of the Aeronautical Sciences, Vol. 21, pp. 690-694 and 706, 1954.

4. Bryson, A. E.: Symmetric Vortex Separation on Circular Cylinders and Cones. Journal of Applied Mechanics, Vol. 26, No. 4, 1959.

5. Schindel, L. H.: Effect of Vortex Separation on Lifting Bodies of Elliptic Cross Section. M.I.T. Aerophysics Laboratory TR 118, September 1965.

6. Pershing, B.: Separated Flow Past Slender Delta Wings with Secondary Vortex Simulation. U.S. Air Force, Space Systems Division, SSD-TDR-64-151, August 1964 (AD 607 442).

7. Squire, L. C.: Camber Effects on the Non-Linear Lift of Slender Wings with Sharp Leading Edge. Aeronautical Research Council ARC 27651, 1966 (AD 483083).

8. Jobe, C. E.: An Aerodynamic Theory of Slender Wings with Leading Edge Separation. Ohio State University, Thesis, 1966.

10. Mangler, K. W., and Smith, J. H. B.: A Theory of the Flow Past a Slender Delta Wing with Leading Edge Separation. Proceedings of the Royal Society, A, Vol. 251, pp. 200-217, 1959. Also: Royal Aircraft Establishment, Report Aero 2593, 1957.

11. Smith, J. H. B.: Improved Calculations of Leading-Edge Separation from Slender Delta Wings. Royal Aircraft Establishment, Technical Report No. 66070, March 1966.

12. Sacks, A. H., et al.: A Theoretical Investigation of the Aerodynamics of Slender Wing-Body Combinations Exhibiting Leading-Edge Separation. NASA Report CR-719, March 1967.

13. Warner, F. J.: On the Solution of "Jury" Problems with Many Degrees of Freedom. Math. Tab., Wash. 11, pp. 268-271, 1957.

14. Levinsky, E. S.; Wei, M. H. Y.; and Strand, T.: Nonlinear Lift of Slender Conical Bodies with Strakes, Air Vehicle Corporation Report No. 352, May 1967.

15. Friberg, E. G.: Measurement of Vortex Separation, Part II: Three Dimensional Circular and Elliptic cones, MIT Aero Lab. Rept. TR 115, August 1965.

16. Fink, P. T.: Some Early Experiments on Vortex Separation, British R & M 3489, 1967.

17. Hummel, D.: Umströmung scharfkantiger schlanker Deltaflügel, Zeitschrift für Flugwissenschaften, 15 Jahrgang, Heft 10, Oct. 1967, pp. 376-385.

TABLE I

EFFECT OF NUMBER OF VORTEX SHEET SEGMENTS

Flat Plate Lift and Isolated Vortex Characteristics, $\alpha/\delta = 0.91$

Number of Vortex Sheet Segments	C_L/δ^2	g_v	y_v	z_v
0 (Linear)	5.7	---	----	----
0 Brown and Michael (ref. 3)	11.2	4.4	0.87	0.22
1 Mangler and Smith (ref. 10)	9.1	3.1	0.80	0.17
3 Present Calculation*	10.1	3.2	0.78	0.21
6 Present Calculation*	10.1	3.3	0.74	0.22
14 Smith (ref. 11)*	9.9	3.2	0.72	0.22

Lift and Isolated Vortex Characteristics Circular Cone, 75% Strakes, $\alpha/\delta = 2.8$

0 Linear	13.7	----	----	----
0 Brown and Michael (Appendix B)	46.0	17.0	0.93	0.50
6 Present Calculation*	39.6	12.2	0.82	0.51
20 Present Calculation**	39.7	8.8	0.81	0.52

* Computed with $\theta_n = 157^\circ$

** $\theta_n = 517^\circ$

TABLE II

SUMMARY OF WING-BODY CALCULATIONS

Body Shape	Strake Size*	Dihedral	α/δ
Flat Plate	----	0^{o}	0.3—8.0
Circle	100%	-10^{o}, 0^{o}, 10^{o}	0.3—8.0
	75%	-10^{o}, 0^{o}, 10^{o}	0.3—8.0
	50%	-10^{o}, 0^{o}, 10^{o}	0.3—8.0
	50%	-20^{o}	5.5—8.0
	25%	-10^{o}, 0^{o}, 10^{o}	0.3—8.0
	10%	-10^{o}, 0^{o}, 10^{o}	0.3—8.0
	0%	40^{o}, 44^{o}, 47^{o}	2.8—8.0
	0%	50^{o}, 53^{o}, 56^{o}	2.8—8.0
Ellipse (a/b = 0.75)	100%	0^{o}	0.3—8.0
	75%	0^{o}	0.3—8.0
	50%	0^{o}	0.3—8.0
	25%	0^{o}	4.0—8.0
	10%	0^{o}	4.0—8.0
Ellipse (a/b = 0.60)	100%	0^{o}	0.3—8.0
	75%	0^{o}	0.3—8.0
	50%	0^{o}	0.3—8.0
	25%	0^{o}	0.3—8.0
	10%	0^{o}	0.3—8.0

* Exposed strake semi span in % of semi major body axis.

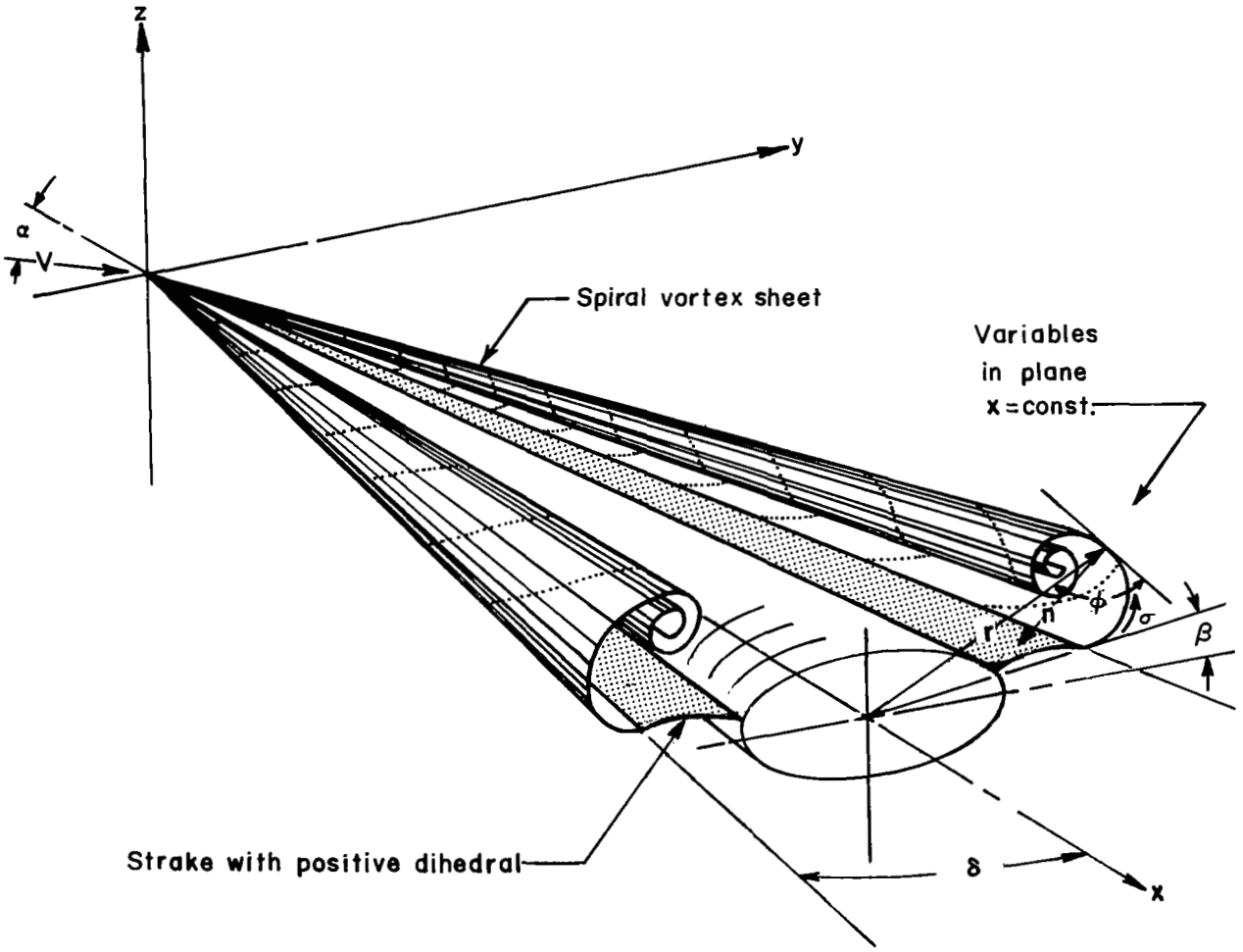

Figure 1. - Conical body-strake configuration.

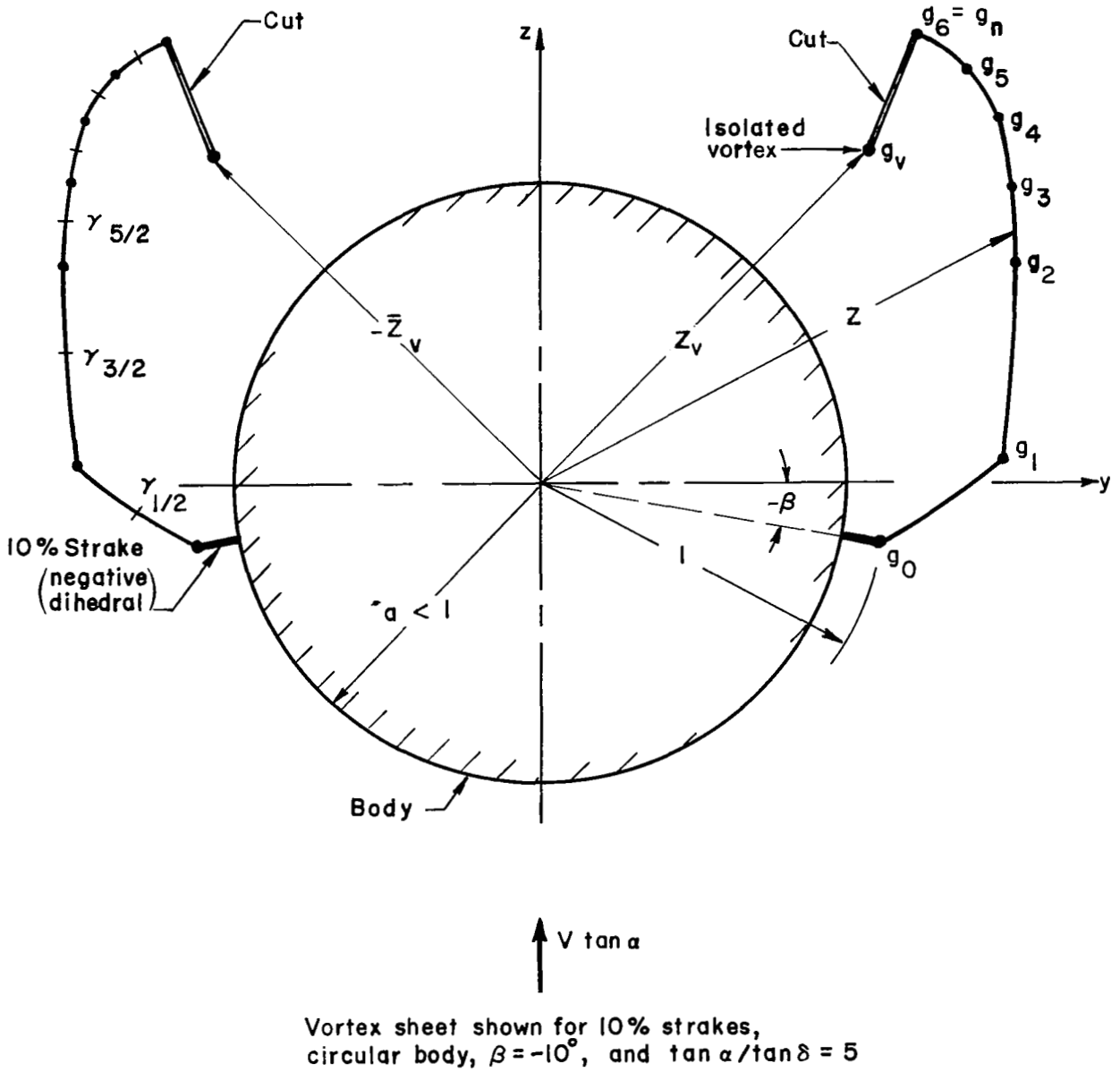

Vortex sheet shown for 10% strakes, circular body, $\beta = -10°$, and $\tan\alpha/\tan\delta = 5$

Figure 2. - Six-segment vortex sheet model, physical cross-flow plane.

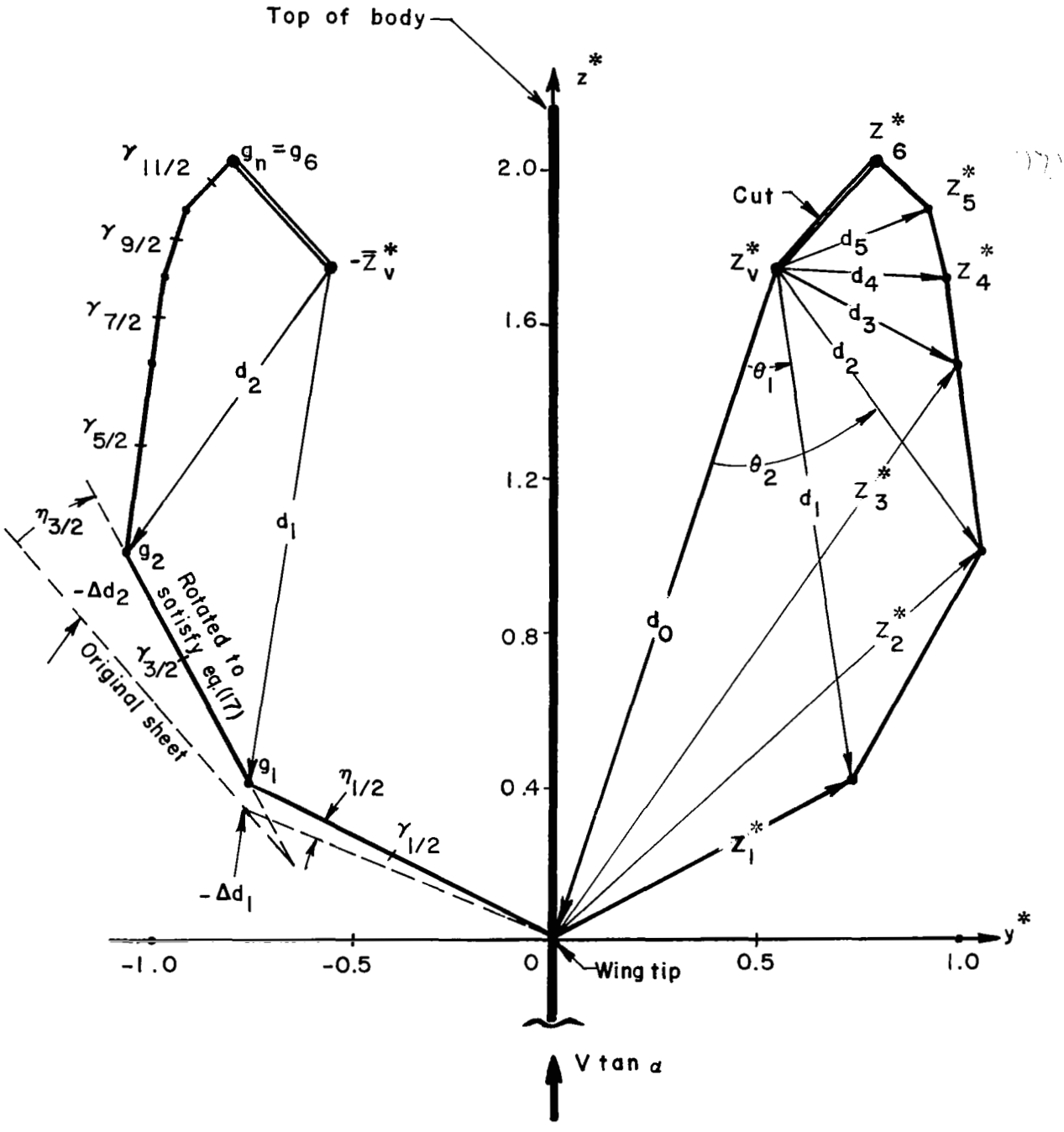

Vortex sheet shown for 10% strakes,
circular body, $\beta = -10°$, and $\tan\alpha / \tan\delta = 5$

Figure 3. - Six-segment vortex sheet model, transformed plane.

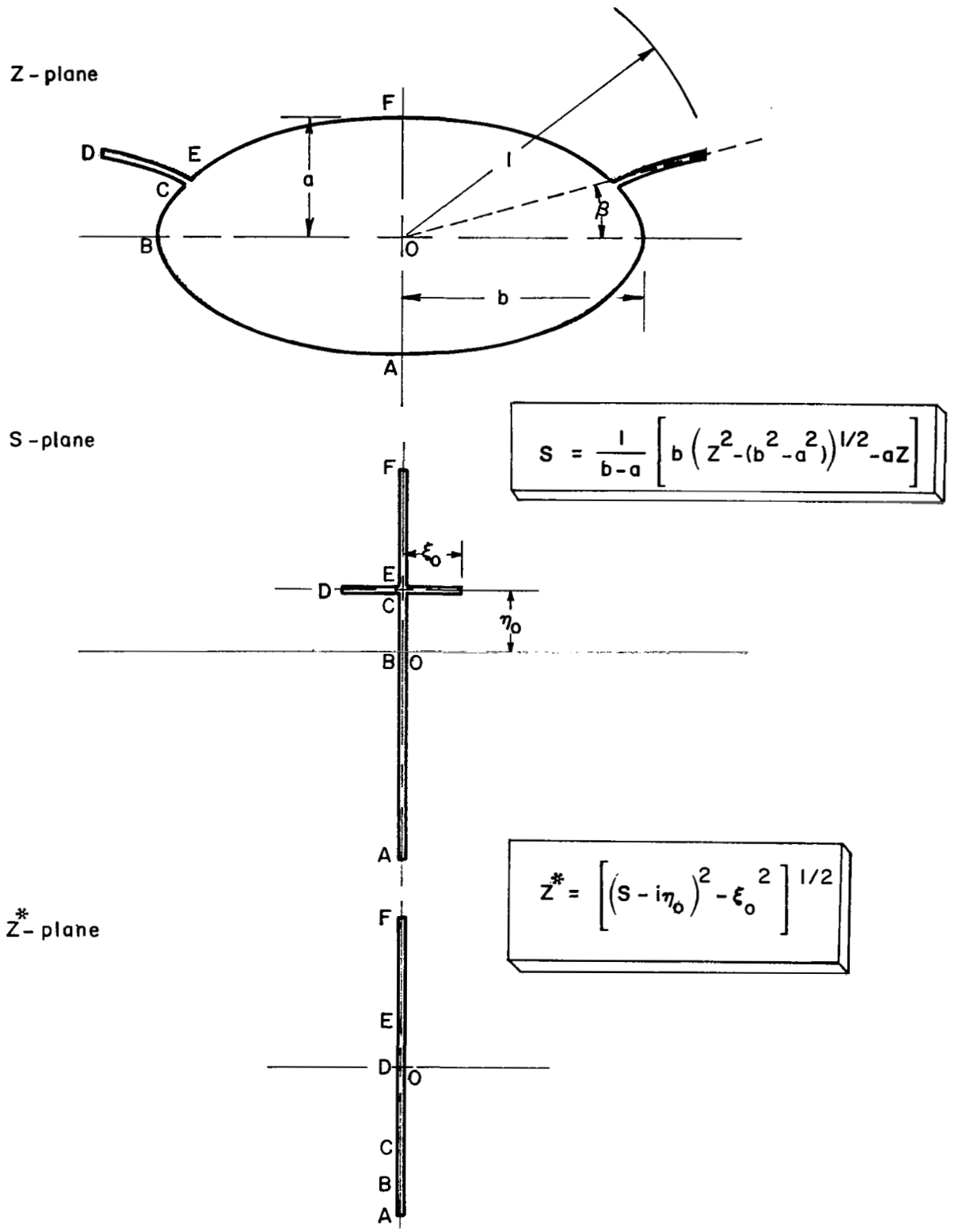

Figure 4. Conformal mapping planes.

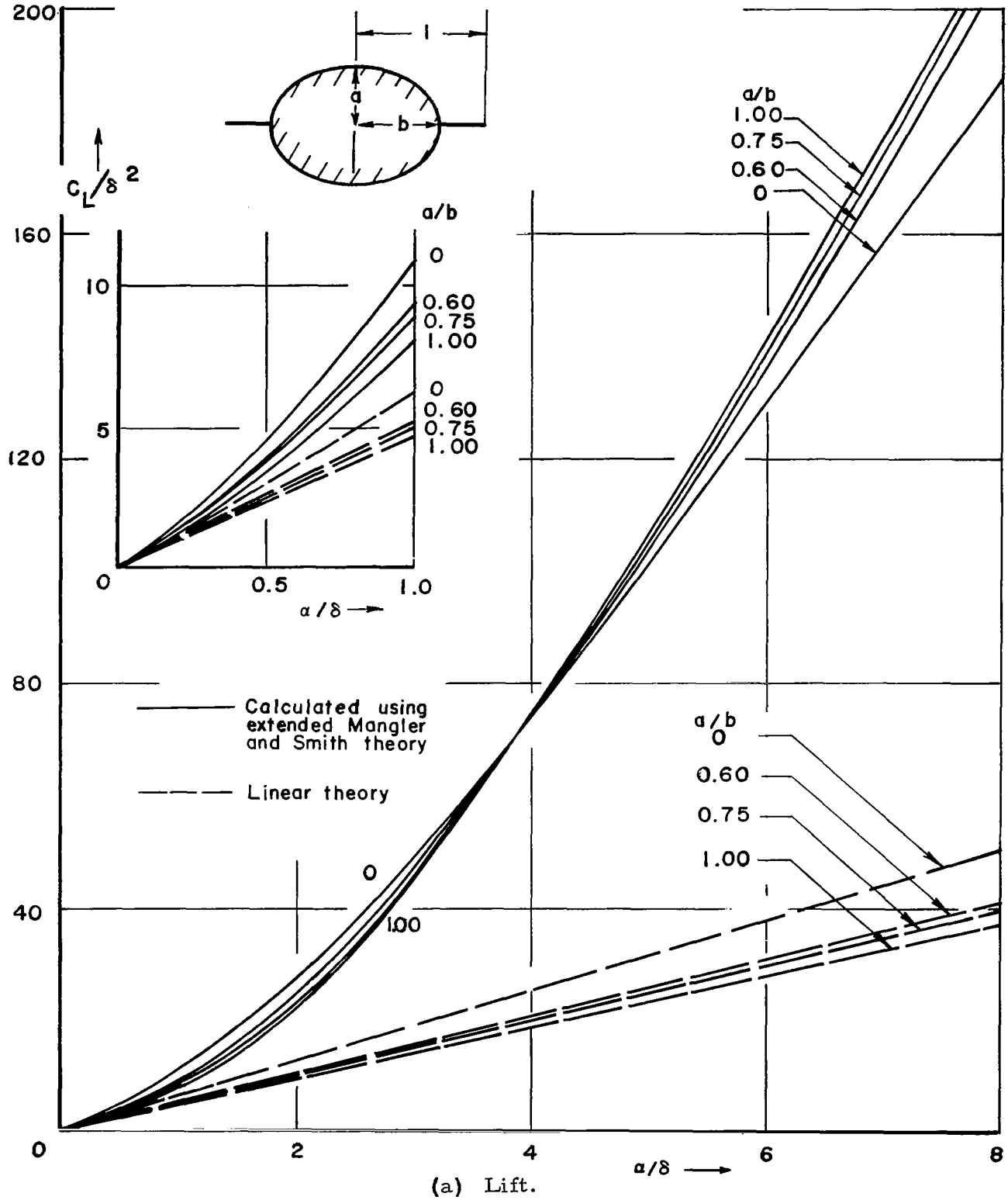

(a) Lift.

Figure 5. - Calculations for cones with 50% strakes, zero dihedral.

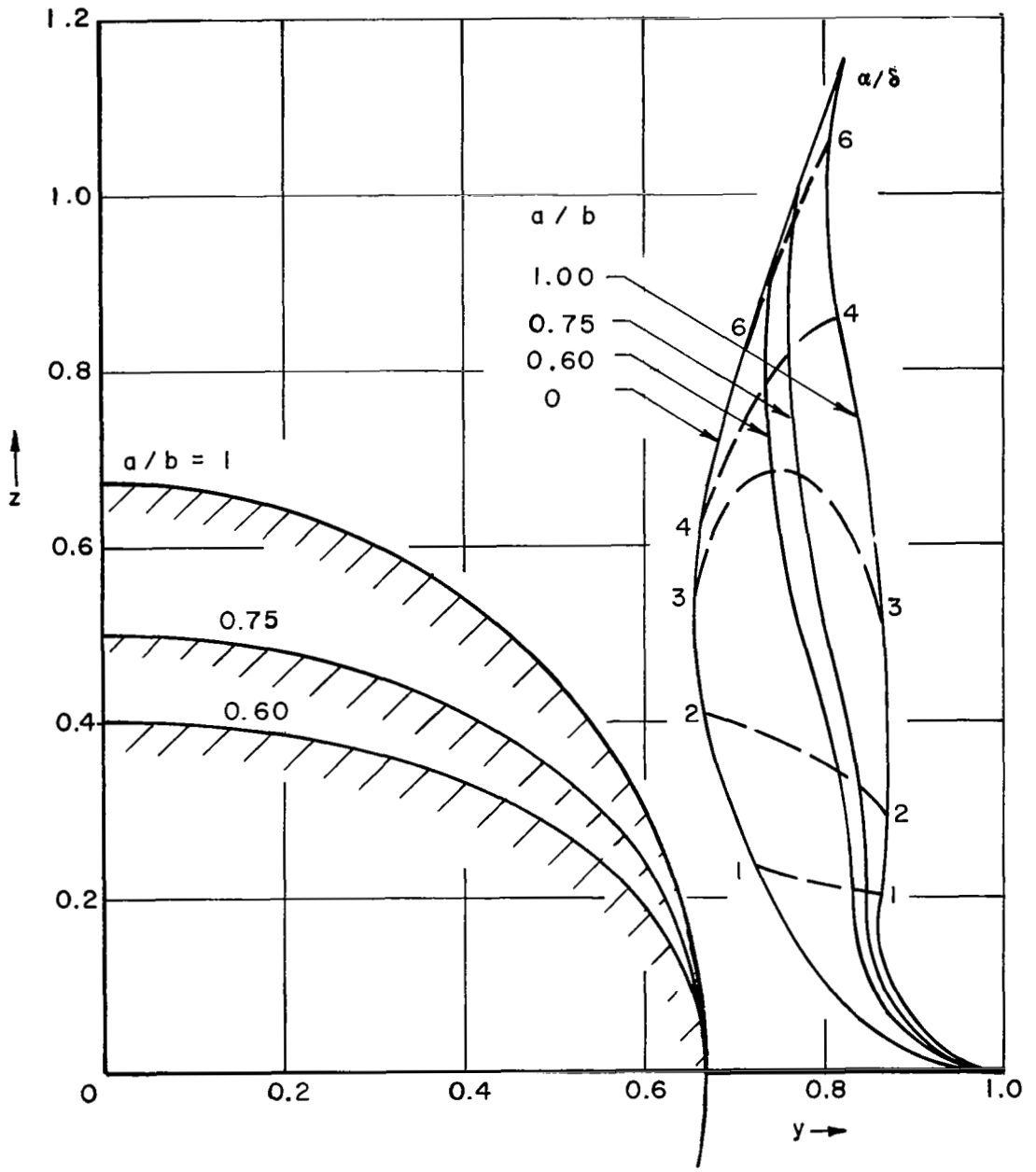

(b) Isolated vortex position.

Figure 5. - Concluded.

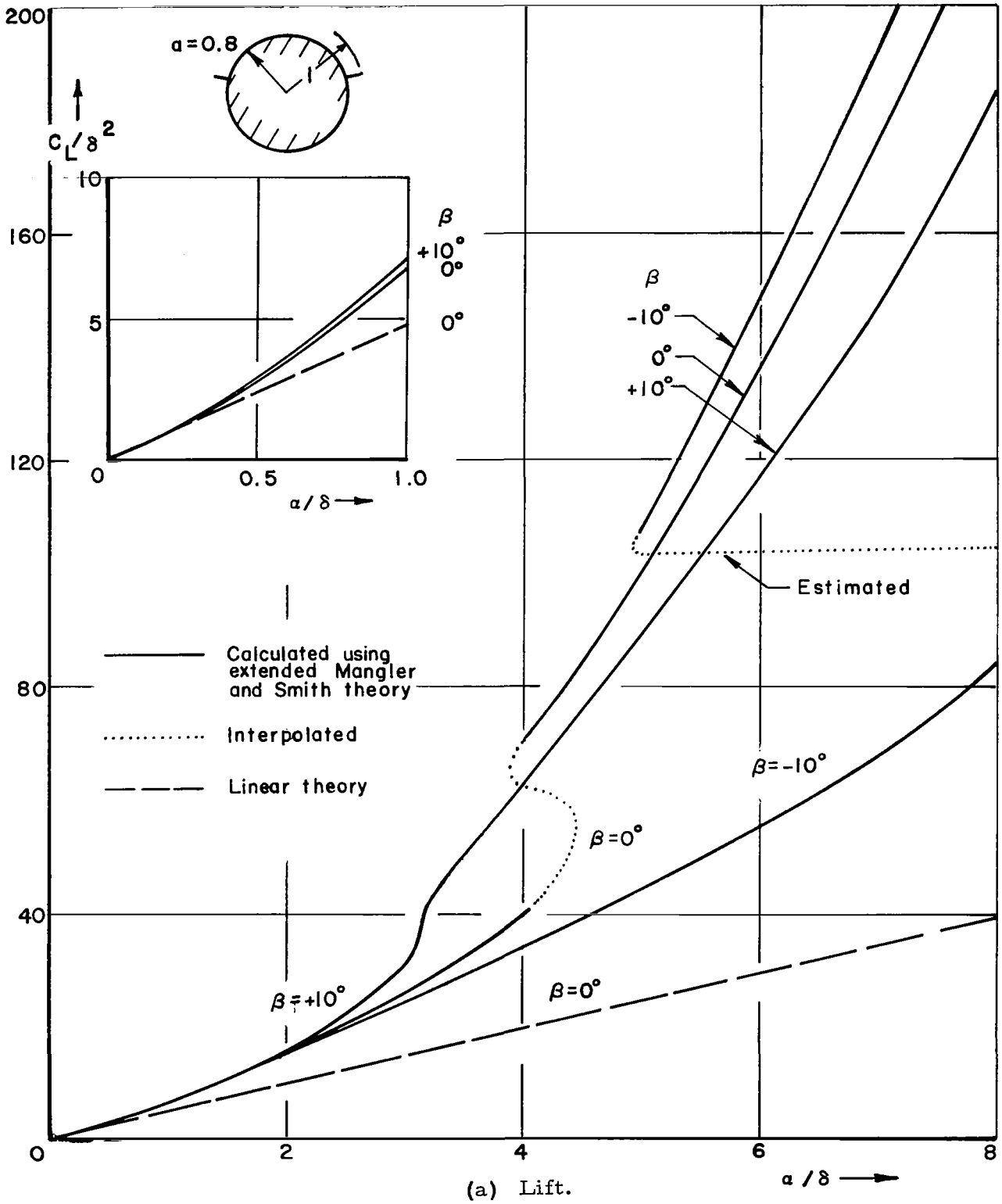

(a) Lift.

Figure 6.- Calculations for cones with 25% strakes.

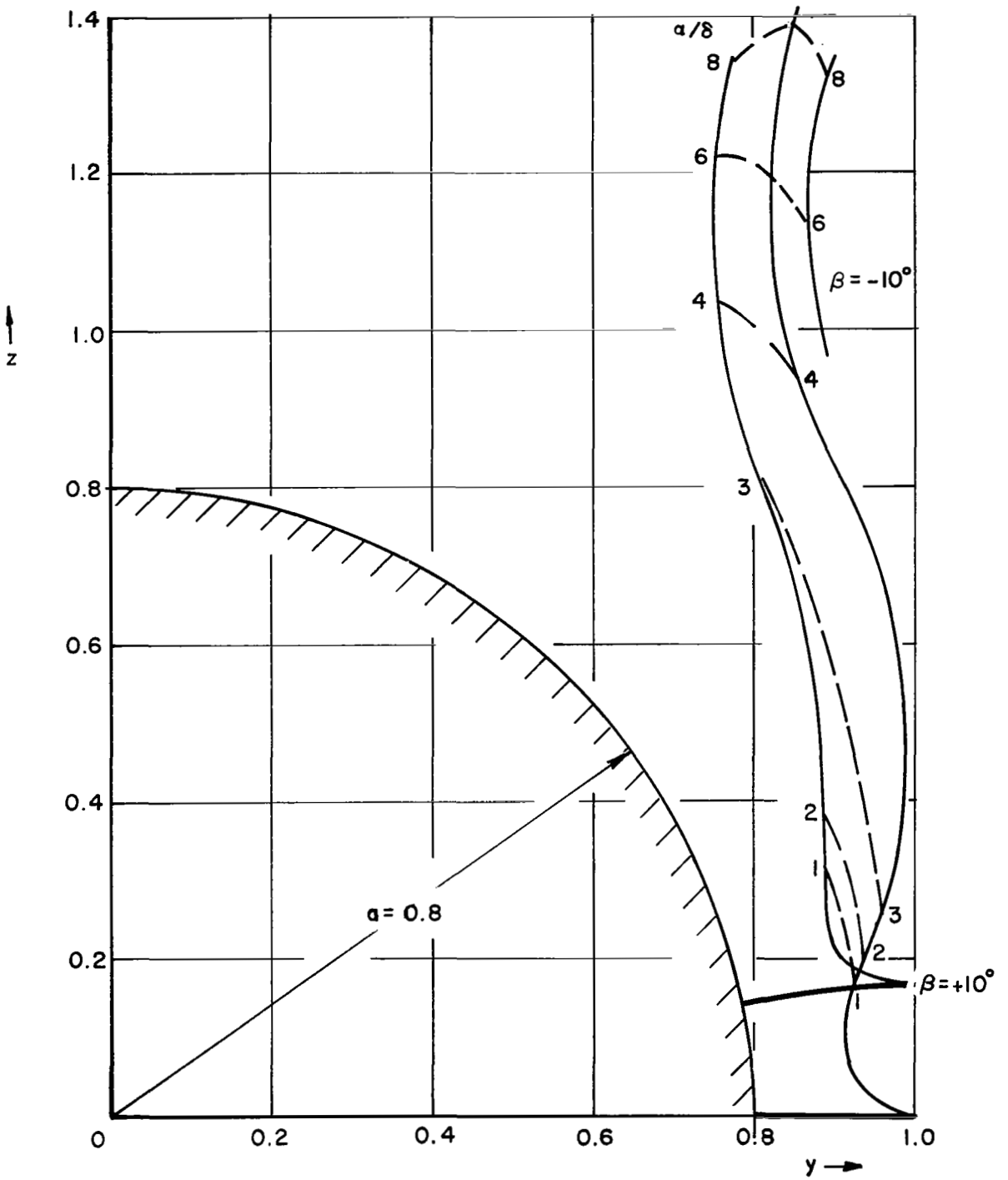

(b) Isolated vortex position.

Figure 6. - Concluded.

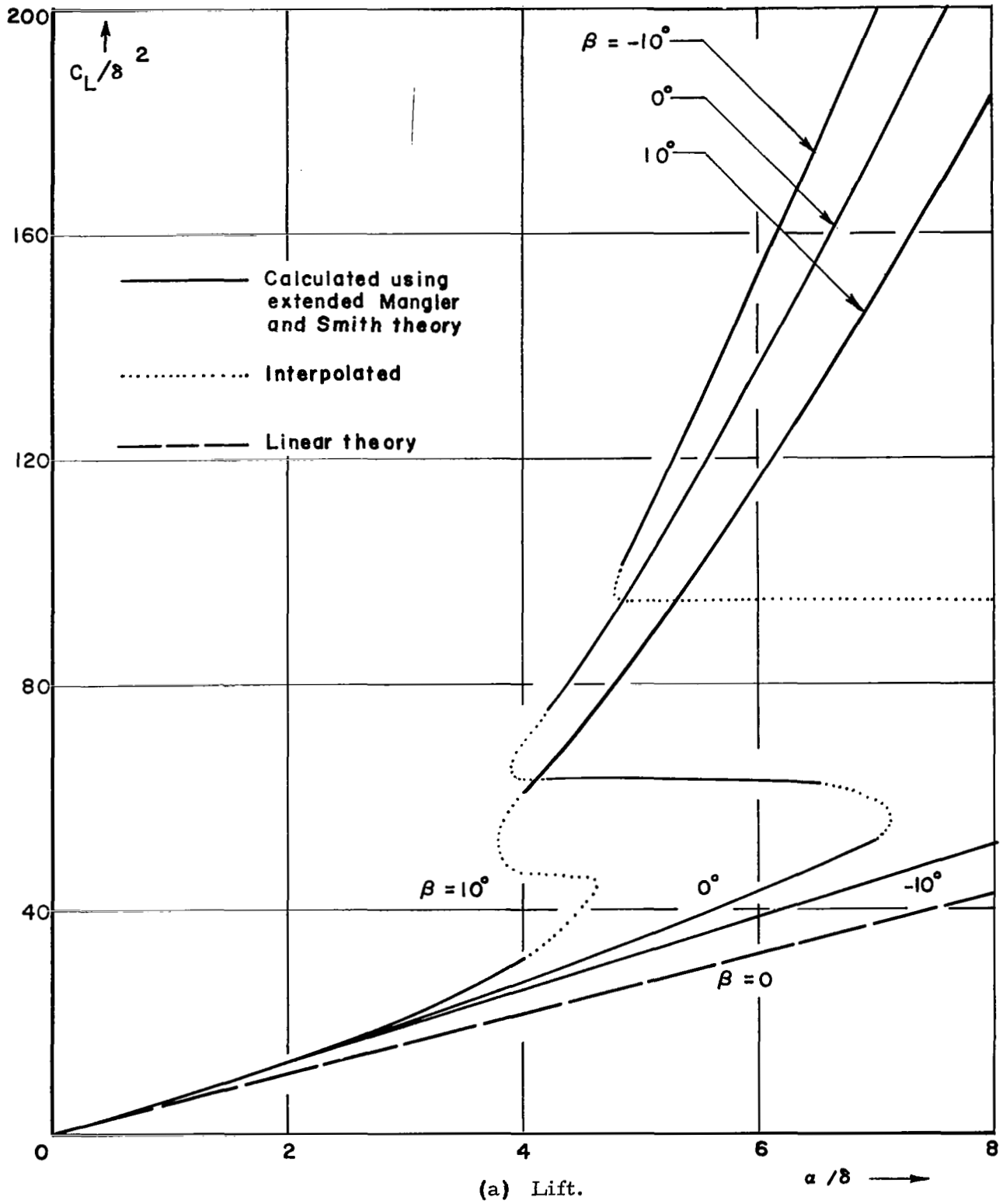

(a) Lift.

Figure 7.- Calculations for cones with 10% strakes.

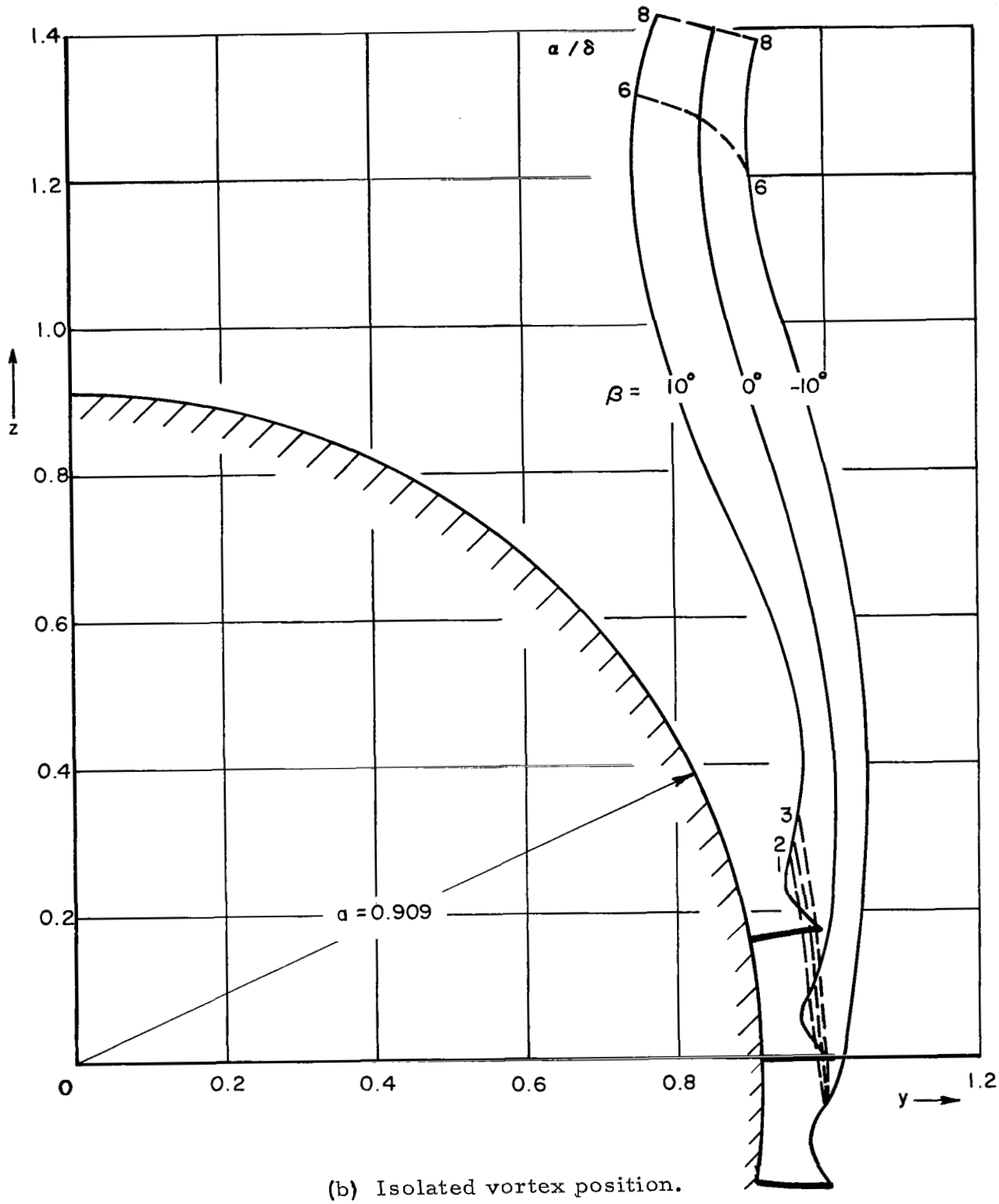

(b) Isolated vortex position.

Figure 7. - Concluded.

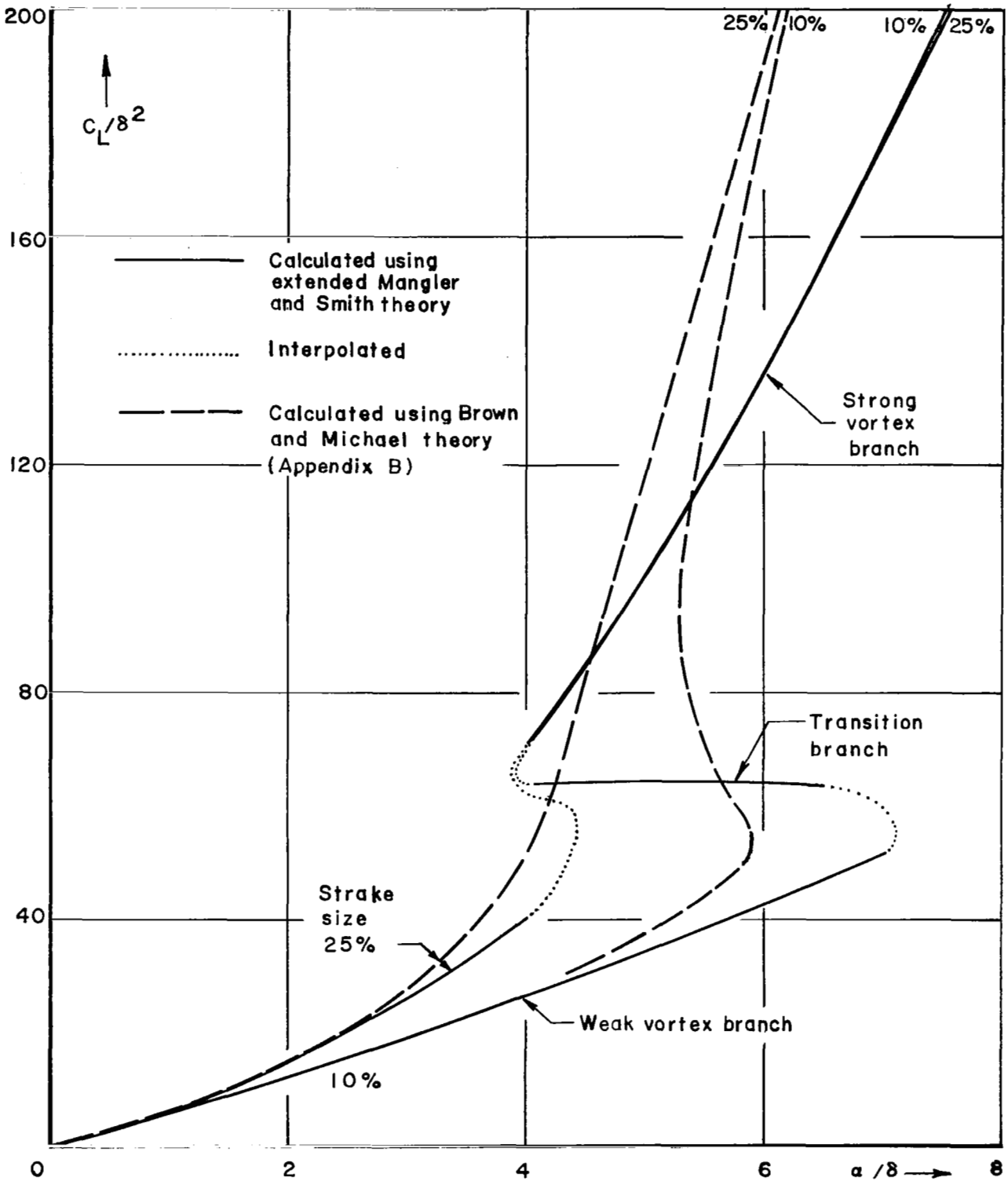

Figure 8. - Comparison with Brown and Michael theory, zero dihedral, circular body.

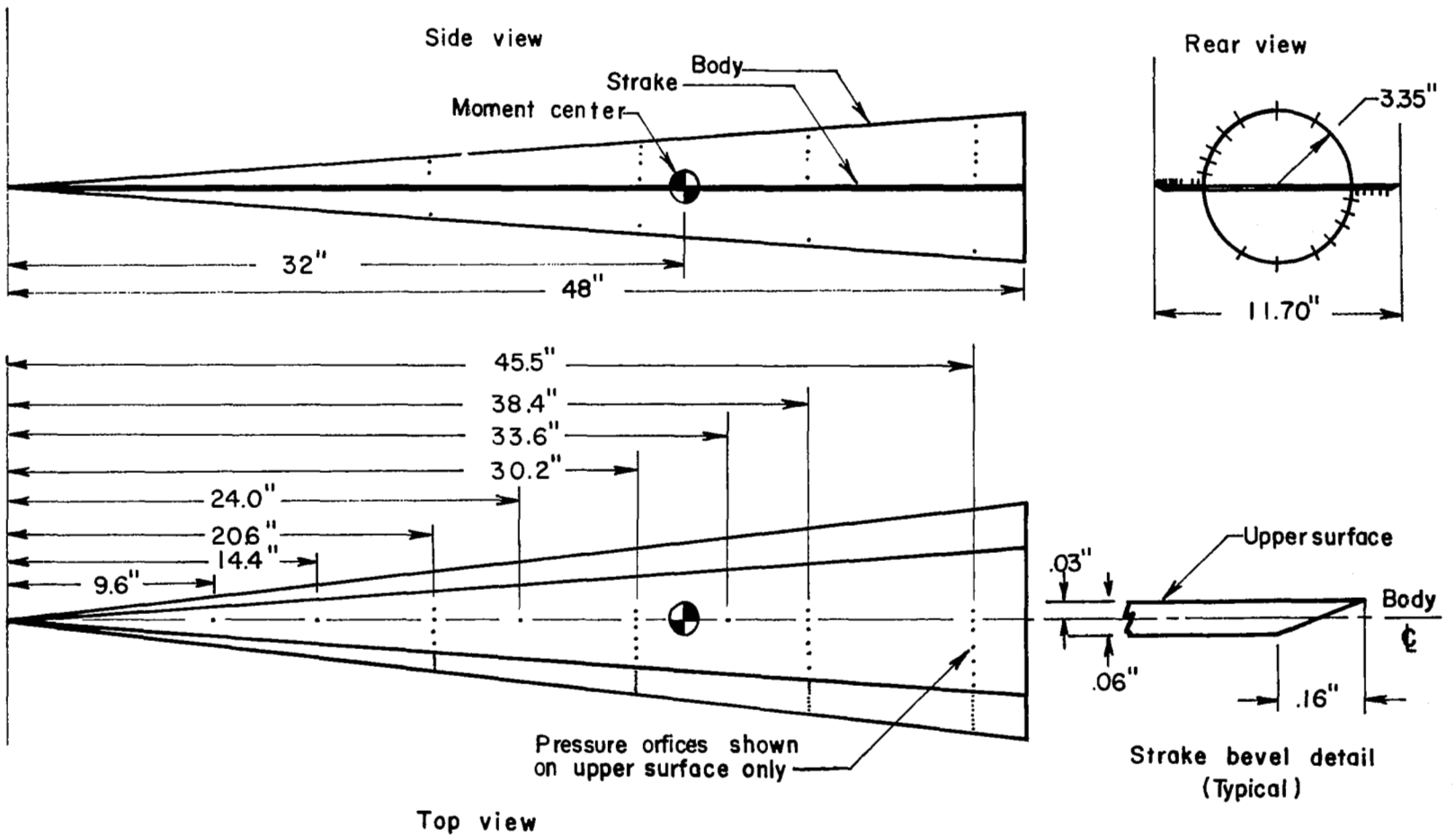

Cone and strakes typical of all models (except for pressure orfices)

Figure 9. - Wind tunnel pressure model, 75% strakes.

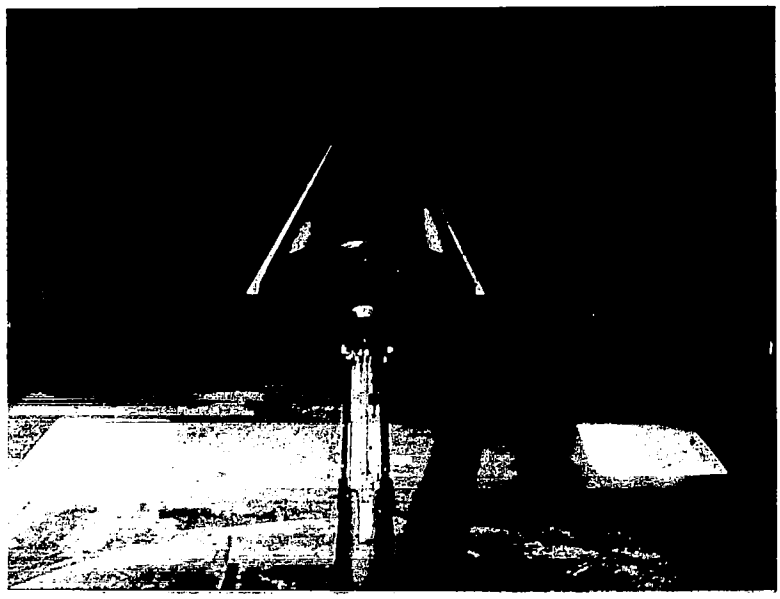

Elliptical cone (a/b =0.6) 10% strakes, α = 16°

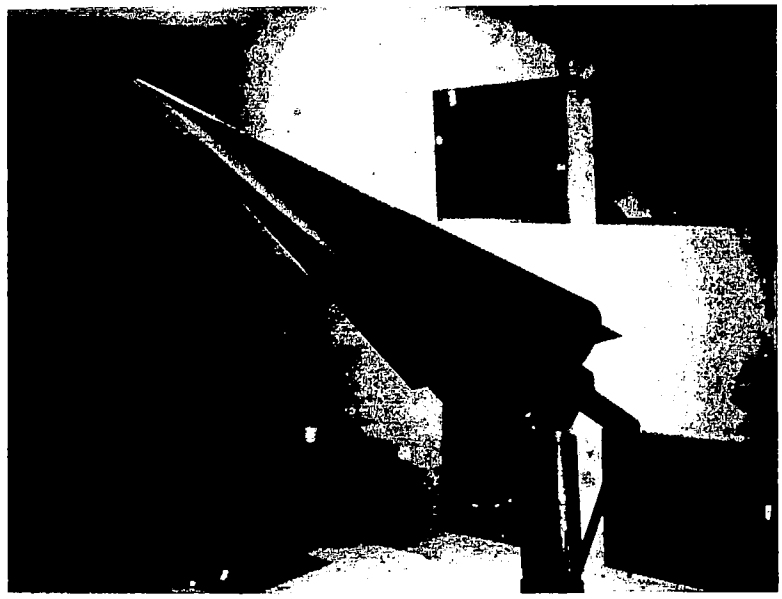

Elliptical cone (a/b =0.6) 50% strakes, α = 28°

Figure 10. - Typical model installations.

	Body no.	δ ~deg	q ~psf	Comments
⊙	2	4.0	75	Yaw + sting extension
⊡	3	6.0	75	" " "
⊡	3	6.0	100	" " "
△	4	8.0	50	" " "
△	4	8.0	75	" " "
◇	5	10.0	50	Pitch with tare correction
◇	5	10.0	75	" " " "

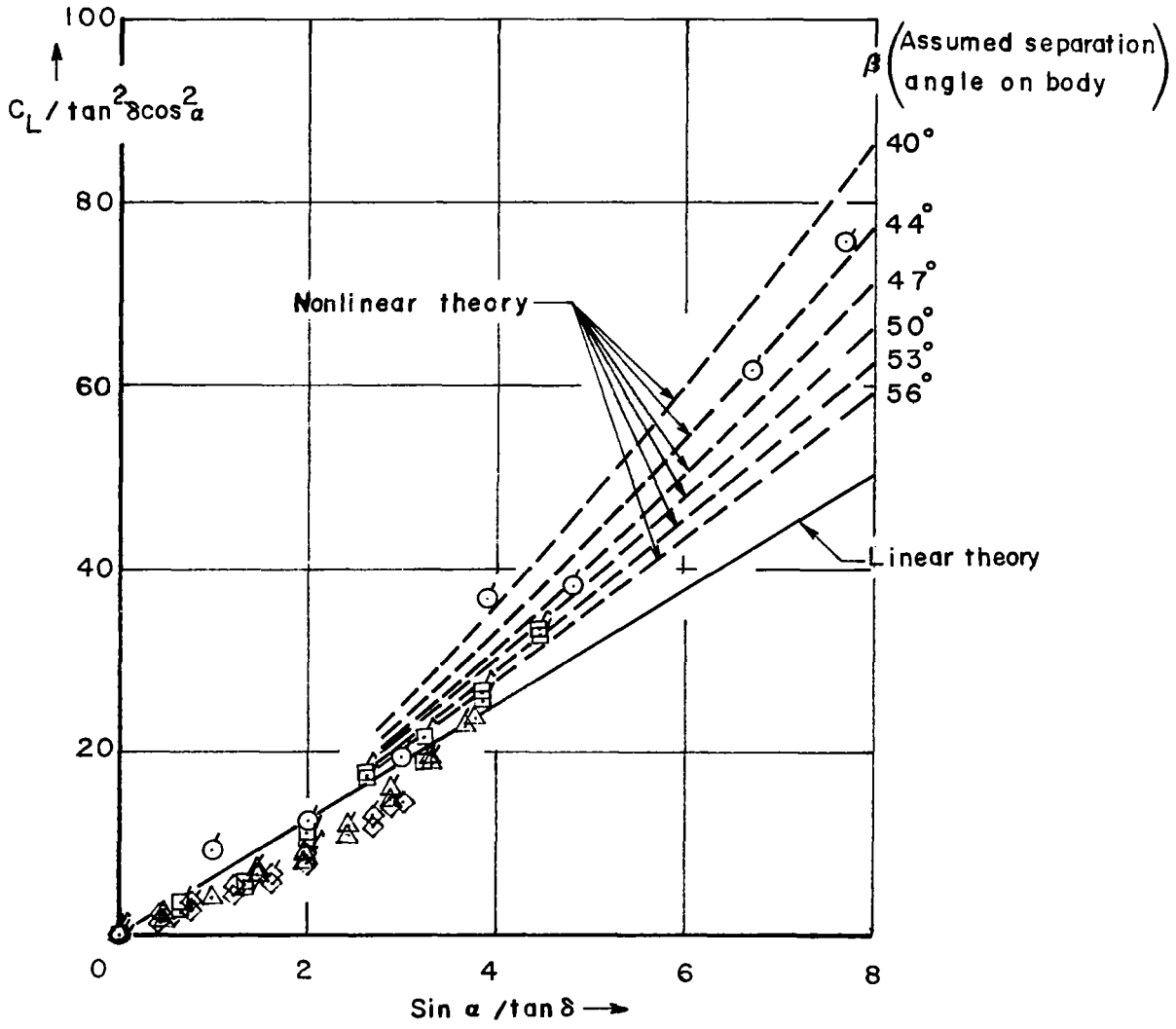

Figure 11.- Comparison of lift data with theory, circular cone without strakes.

	Body no.	δ ~deg	q ~psf	Comments
⊙	2	4.4	75	Yaw + sting extension
⊙	2	4.4	100	" " "
⊡	3	6.6	75	" " "
⊡	3	6.6	100	" " "
△	4	8.8	50	" " "
△	4	8.8	75	" " "
◇	5	11.0	50	Pitch with tare correction
◇	5	11.0	75	" " " "

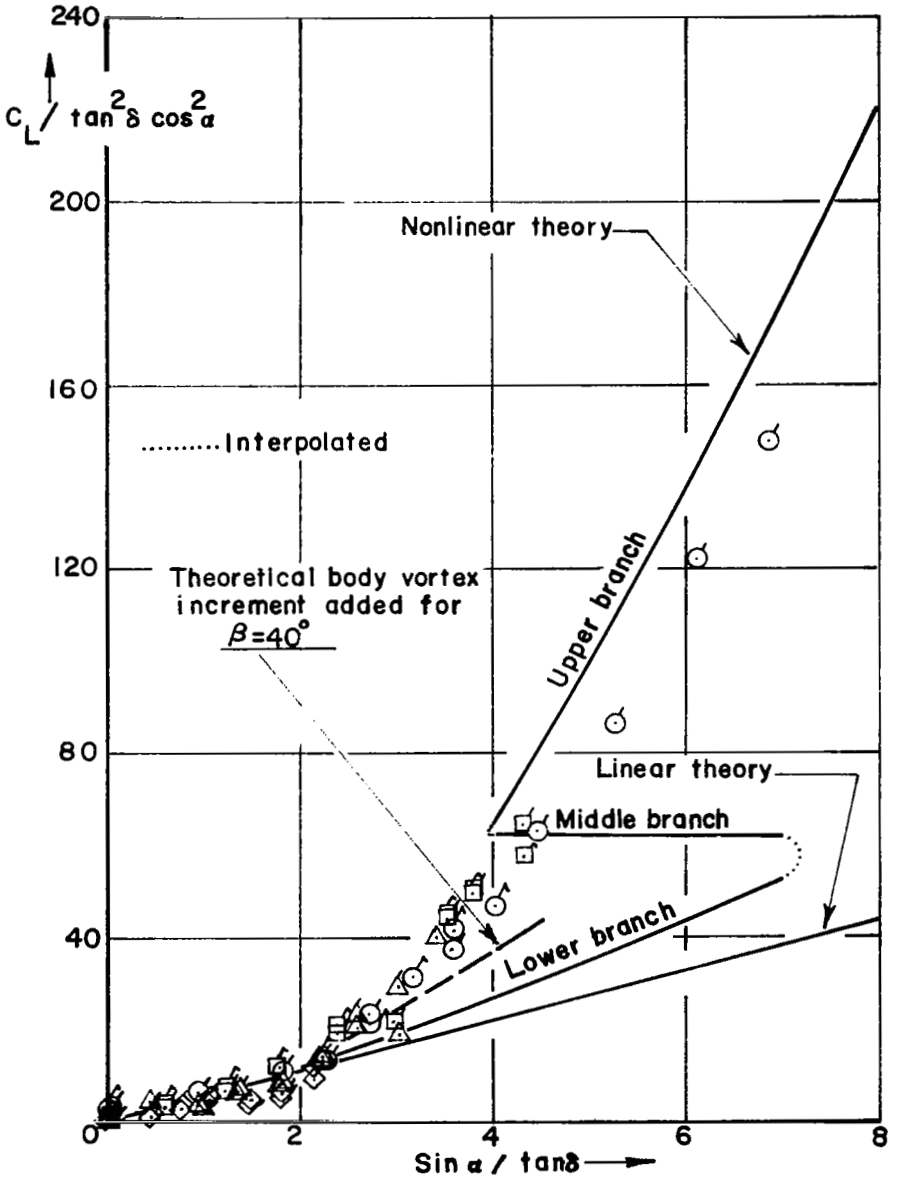

Figure 12. - Comparison of lift data with theory, circular cone, 10% strakes.

Body no.	δ ~deg	q ~psf	Comments
2	5.0	75	Yaw+sting extension
2	5.0	100	" " "
3	7.5	75	" " "
3	7.5	100	" " "
4	10.0	50	" " "
4	10.0	75	" " "

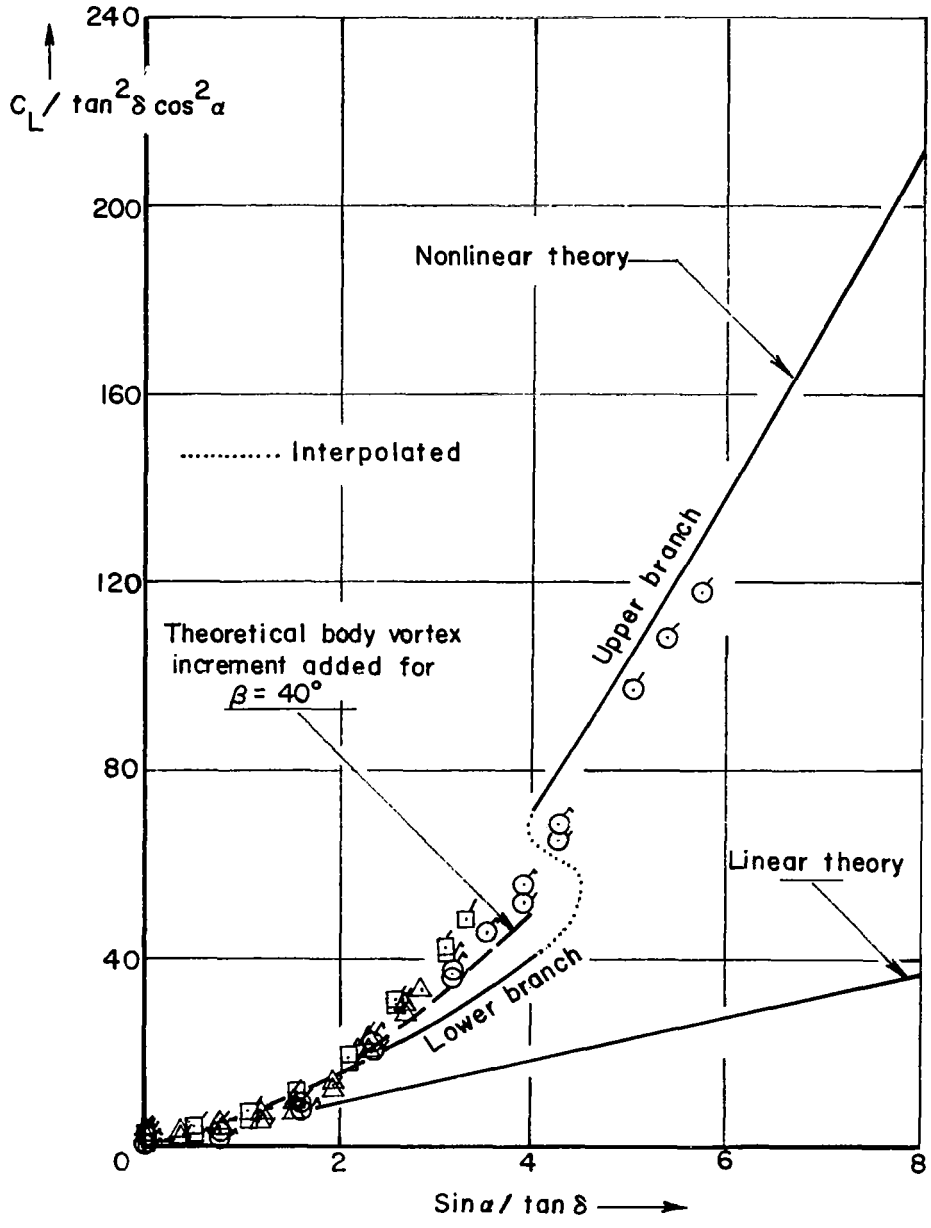

Figure 13. - Comparison of lift data with theory, circular cone, 25% strakes.

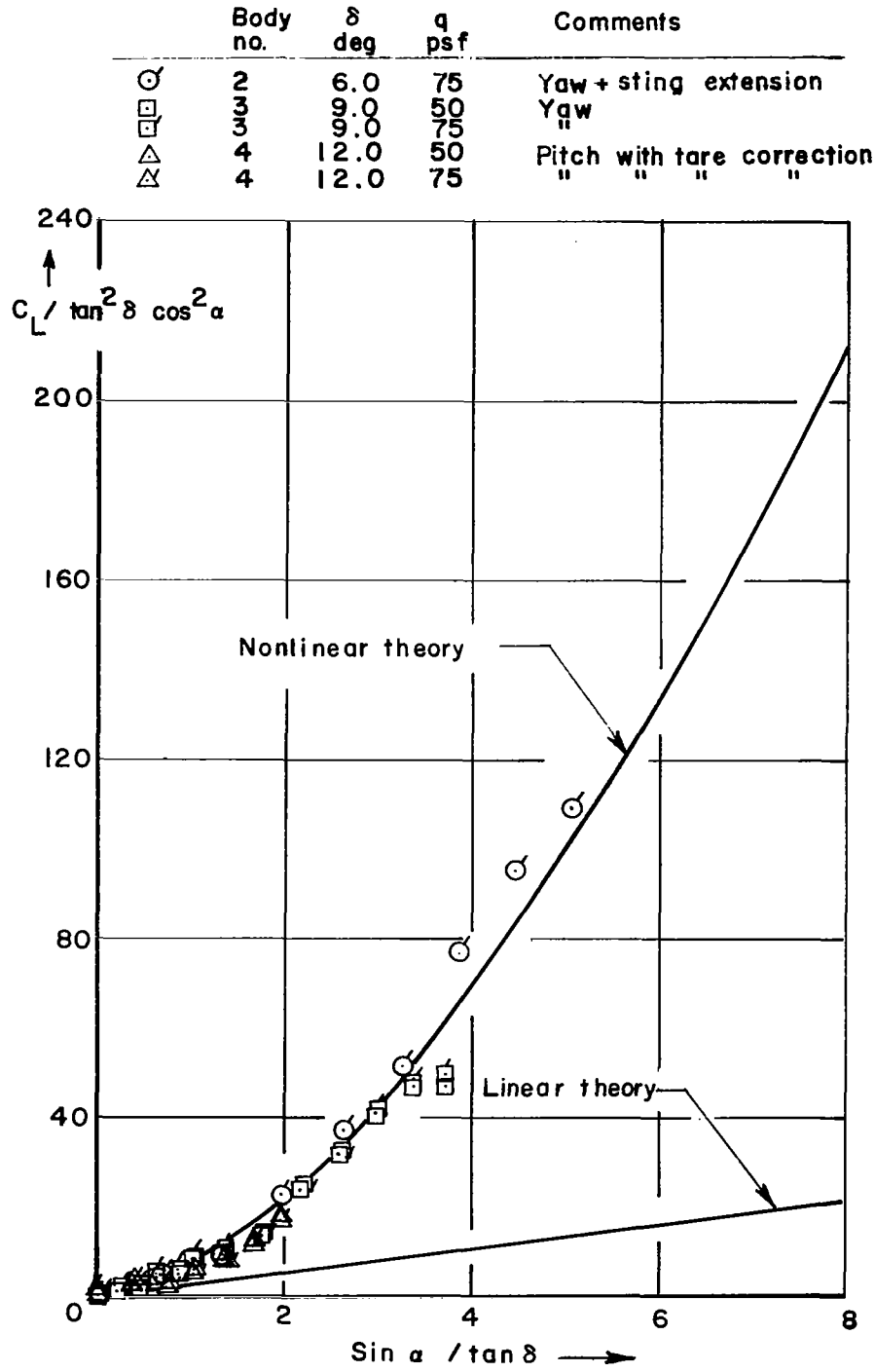

Figure 14. - Comparison of lift data with theory, circular cone, 50% strakes.

	Body no.	δ ~deg	q ~psf	Comments
⊙	2	7.0	75	Yaw+sting extension
⊡	3	10.5	50	Yaw
⊡	3	10.5	75	"
△	4	14.0	50	Pitch with tare correction
△	4	14.0	75	" " " "

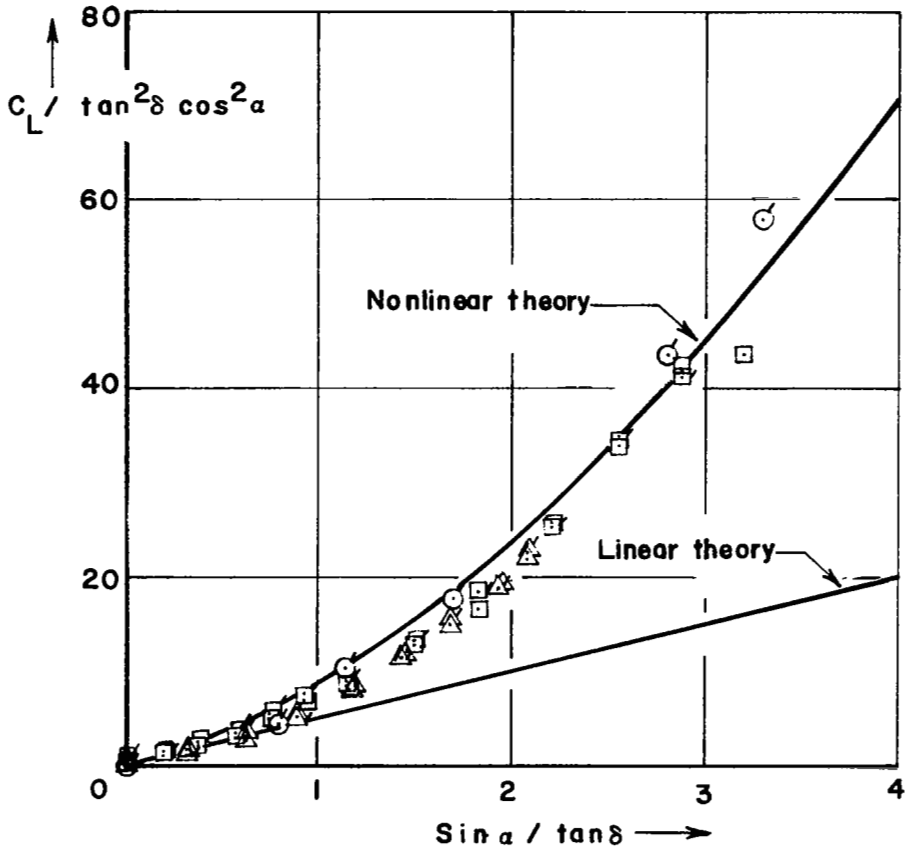

Figure 15. - Comparison of lift data with theory, circular cone, 75% strakes.

	Body no.	δ ~deg	q ~psf	Comments
⊙	2	8.0	75	Yaw+sting extension
⊡	3	12.0	50	Yaw
⊡	3	12.0	75	"
△	4	16.0	50	Pitch with tare correction
△	4	16.0	75	" " " "

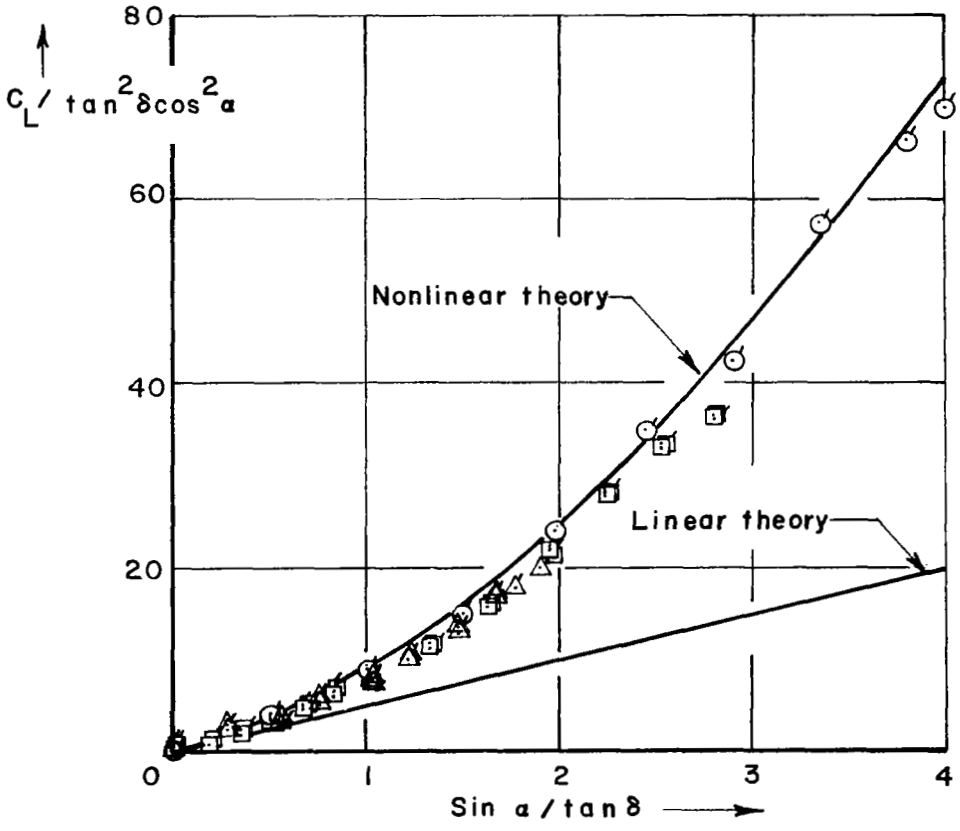

Figure 16. - Comparison of lift data with theory, circular cone, 100% strakes.

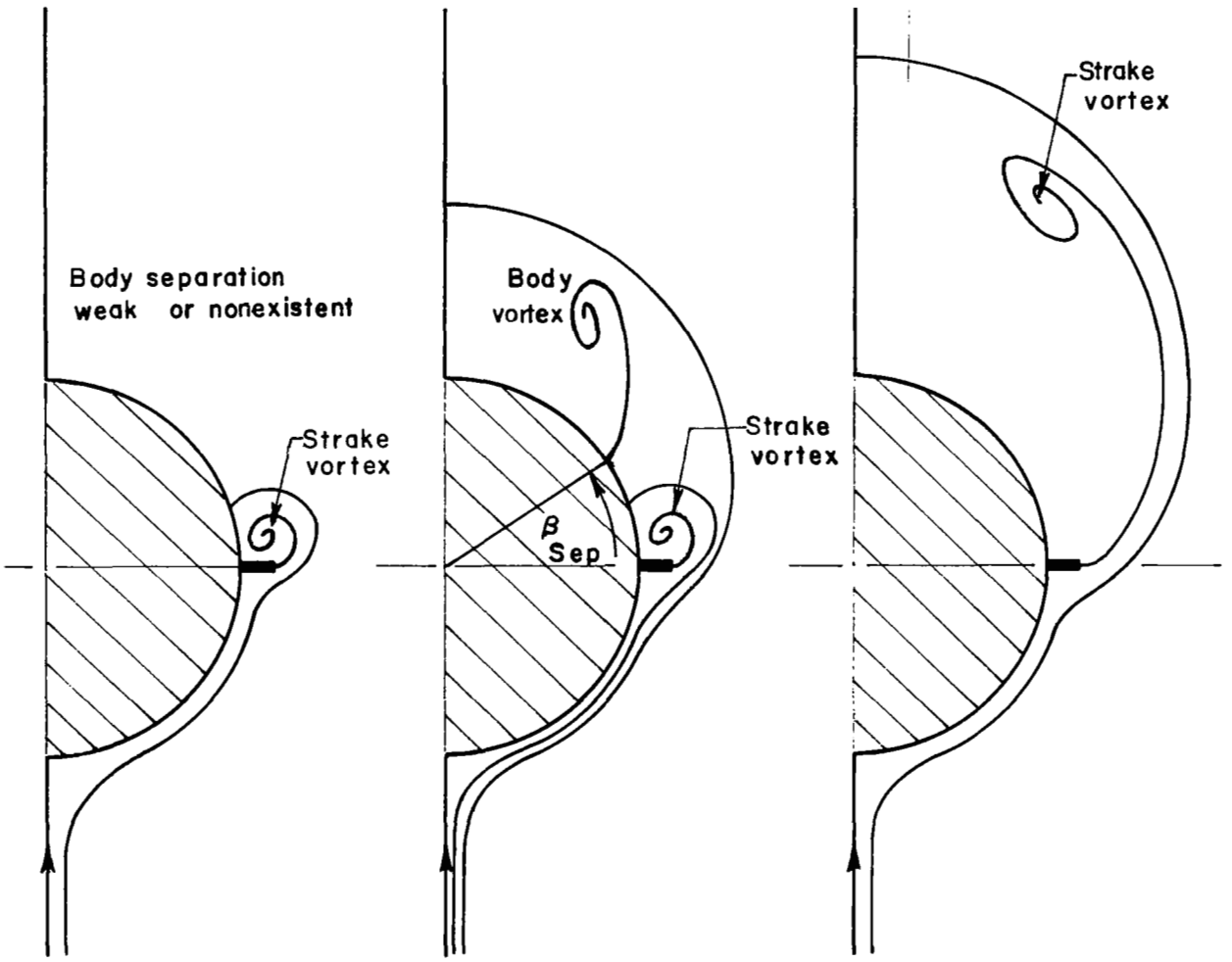

Figure 17.- Formation of body vortices on a cone with small strakes.

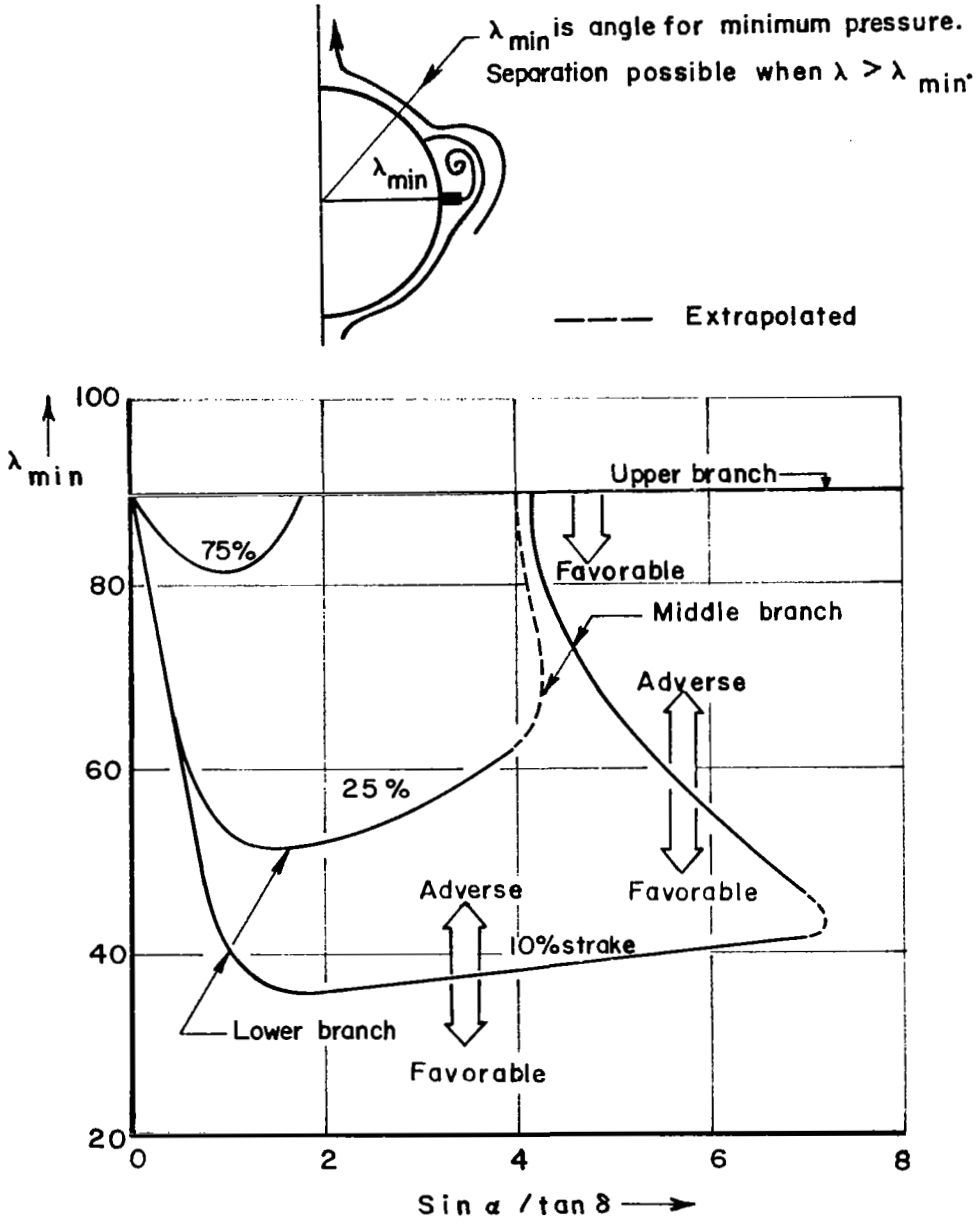

Figure 18. - Calculated regions of adverse pressure gradient.

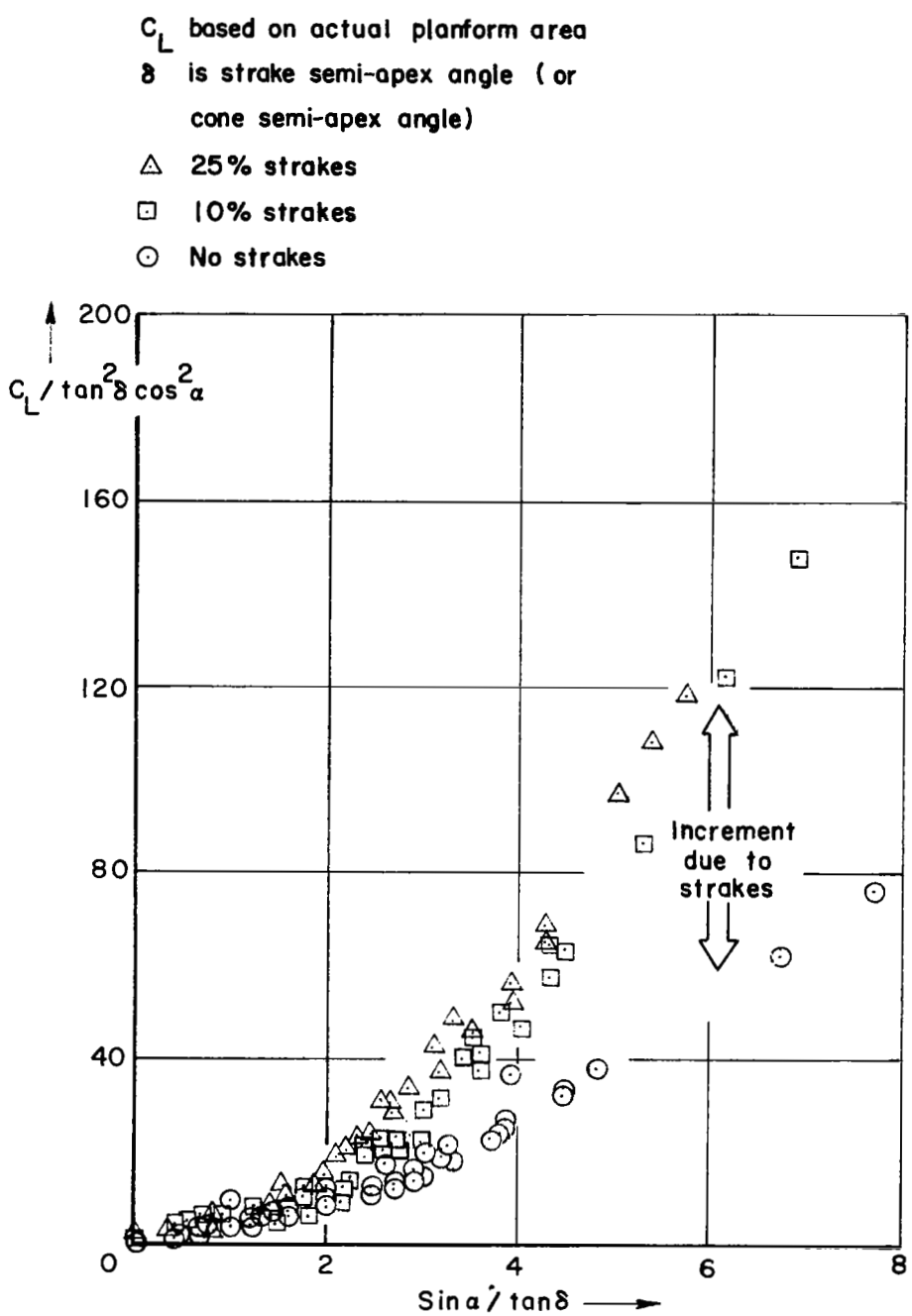

Figure 19. Lift gain with small strakes on circular cones.

	Body no.	δ ~deg	q ~psf	Comments
▽	6	11.0	50	Pitch with tare correction
▽	6	11.0	75	" " " "

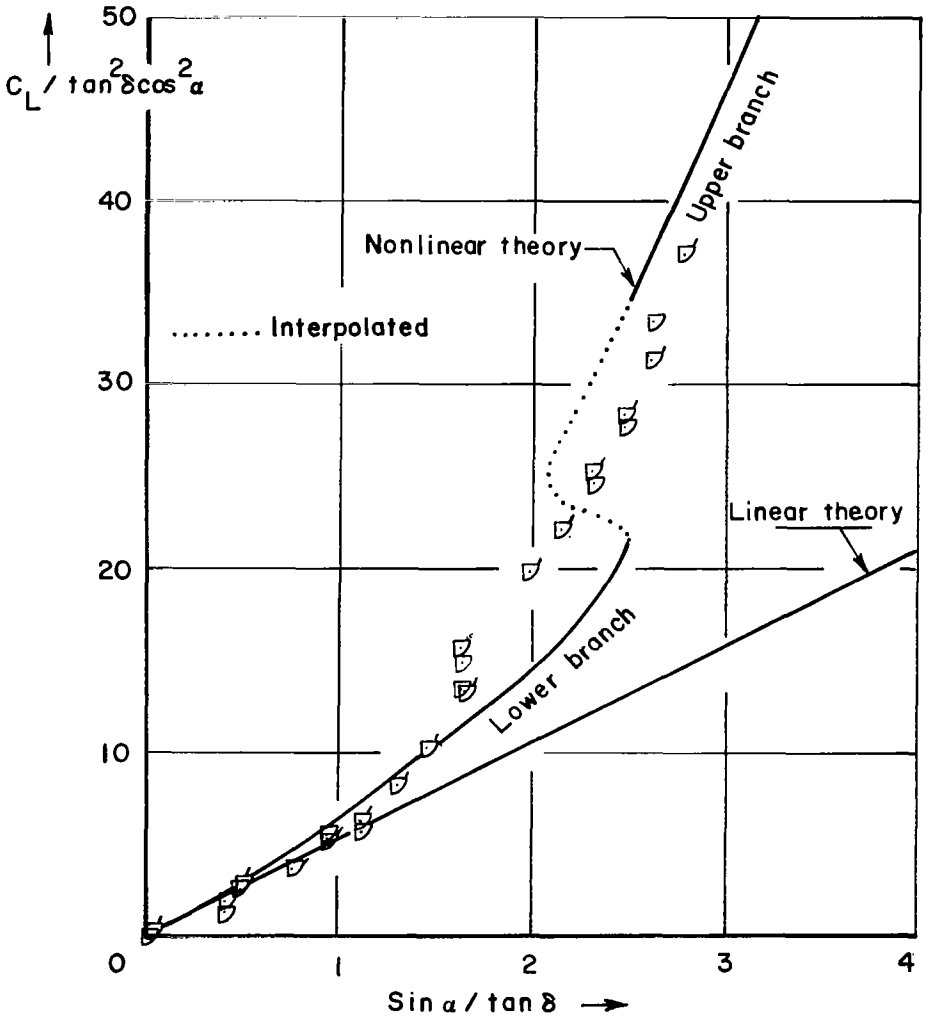

Figure 20. Comparison of lift data with theory
a/b = 0.6 elliptical cone, 10% strakes.

Body no.	δ ~deg	q ~psf	Comments
6	12.4	50	Pitch with tare correction
6	12.4	75	" " " "

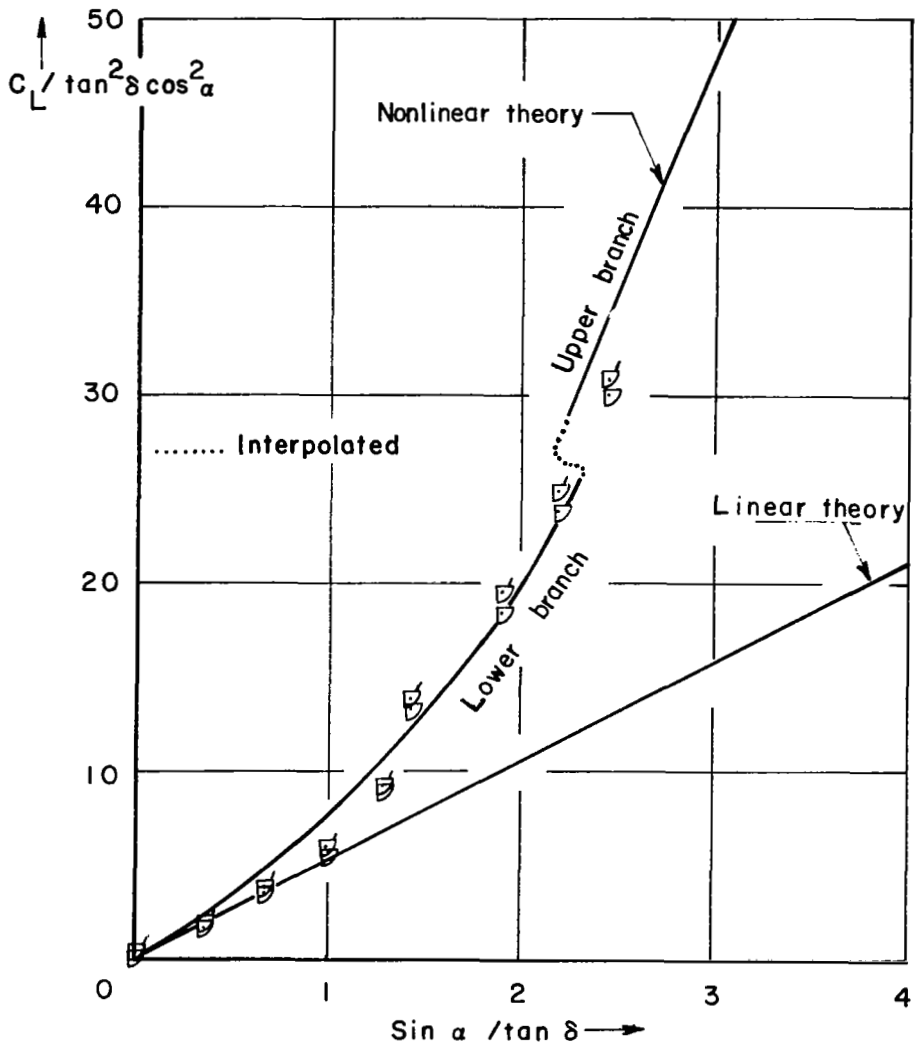

Figure 21. Comparison of lift data with theory
a/b = 0.6 elliptical cone, 25% strakes.

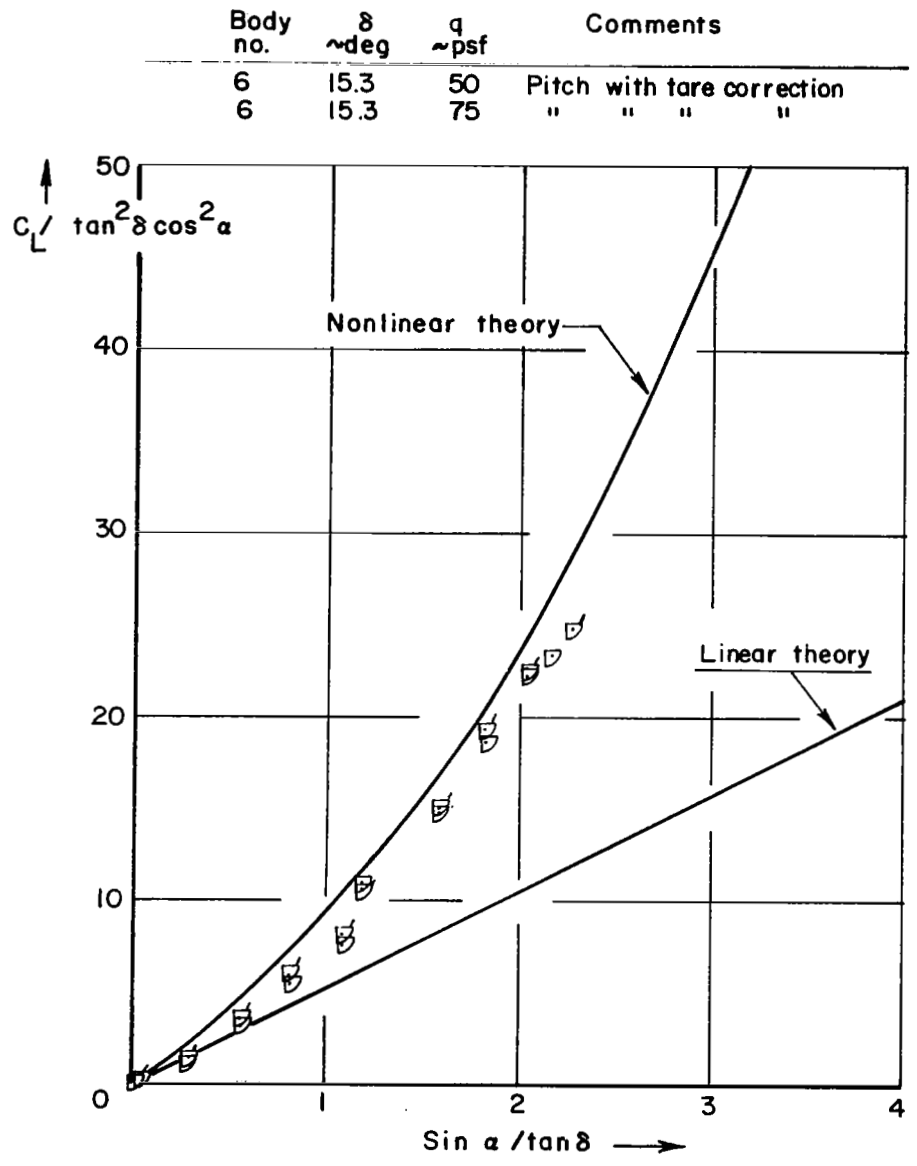

Figure 22. Comparison of lift data with theory a/b = 0.6 elliptical cone, 50% strakes.

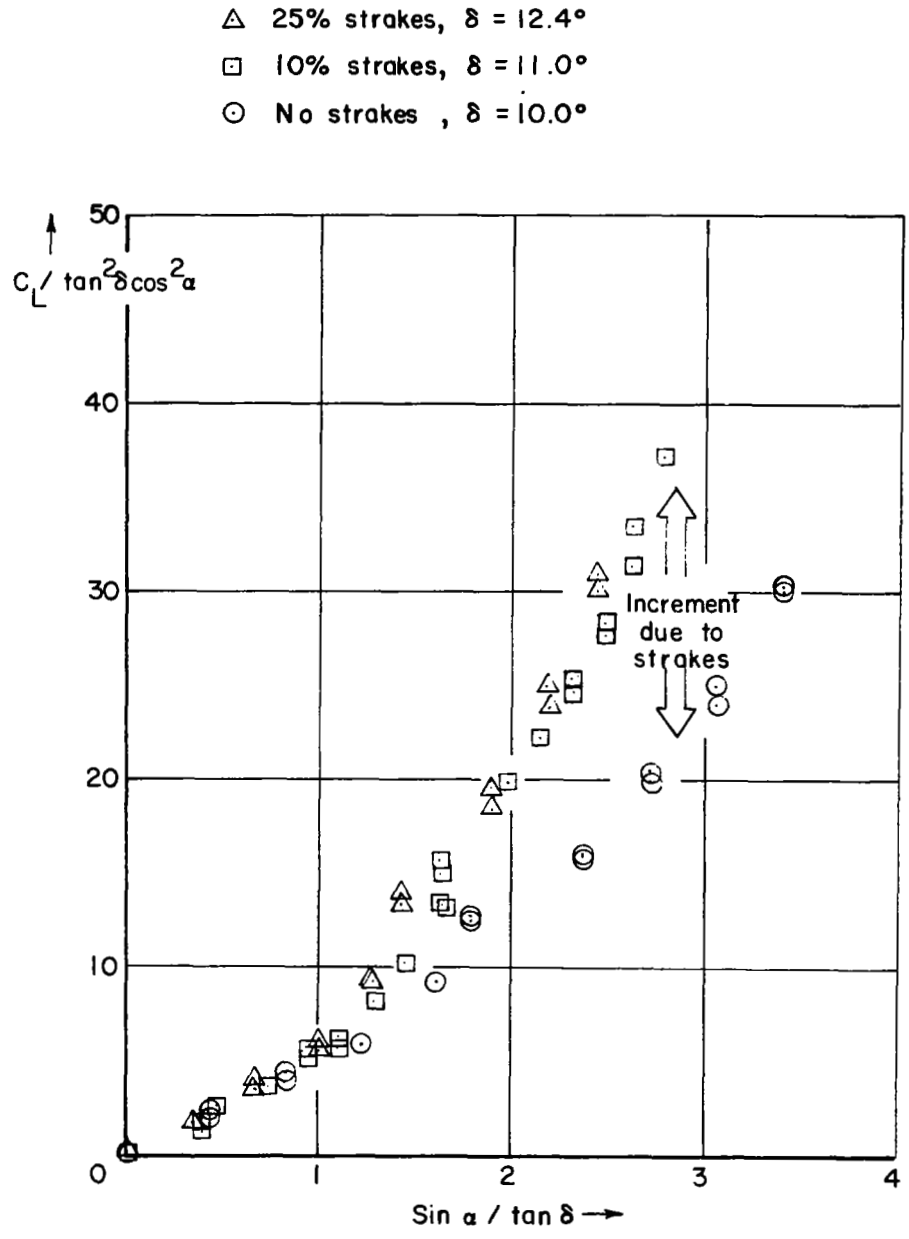

Figure 23. Lift gain with small strakes on a/b = 0.6 elliptical cone.

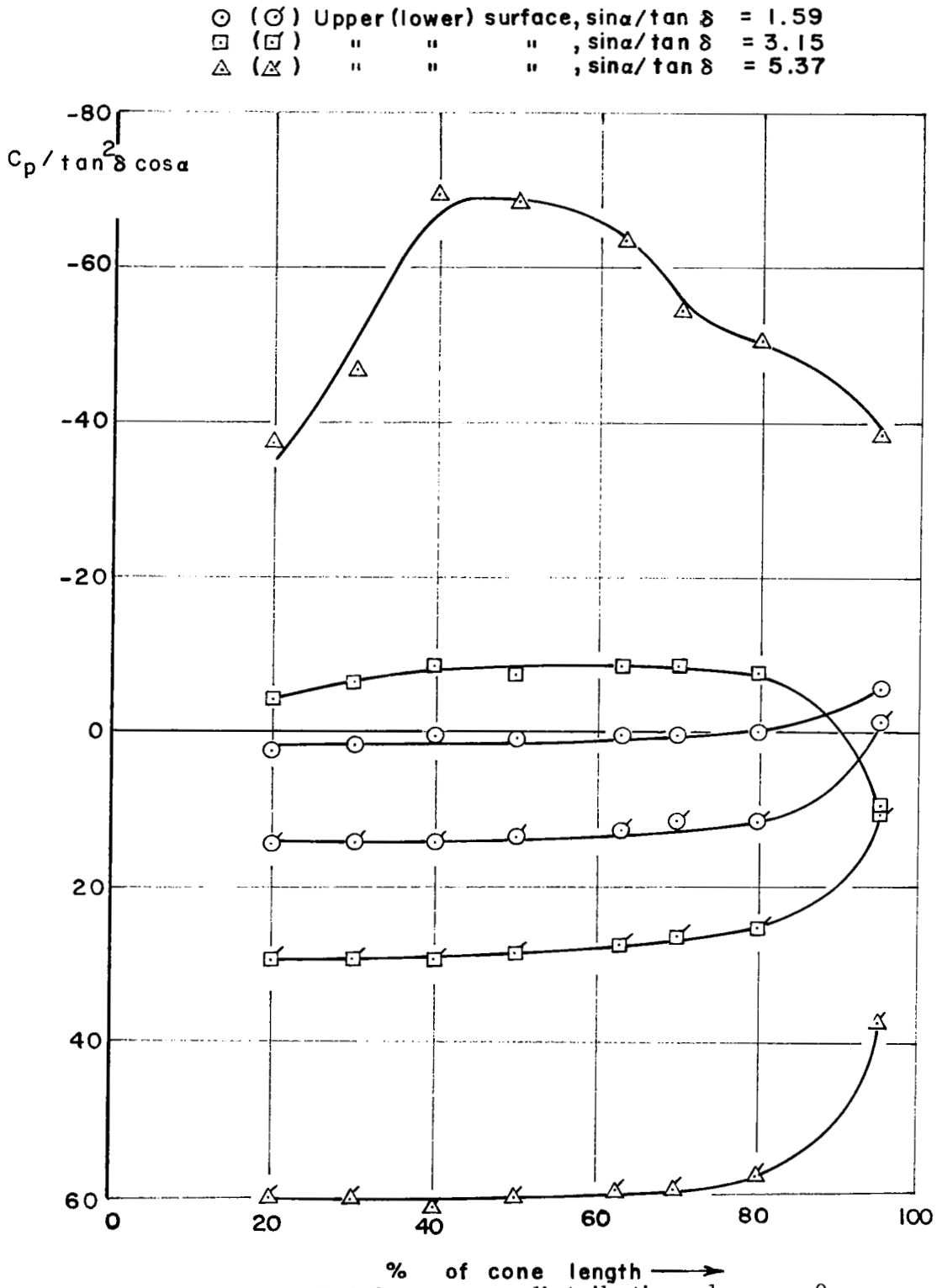

Figure 24. - Axial pressure distribution along y = 0, circular cone with 25% strakes.

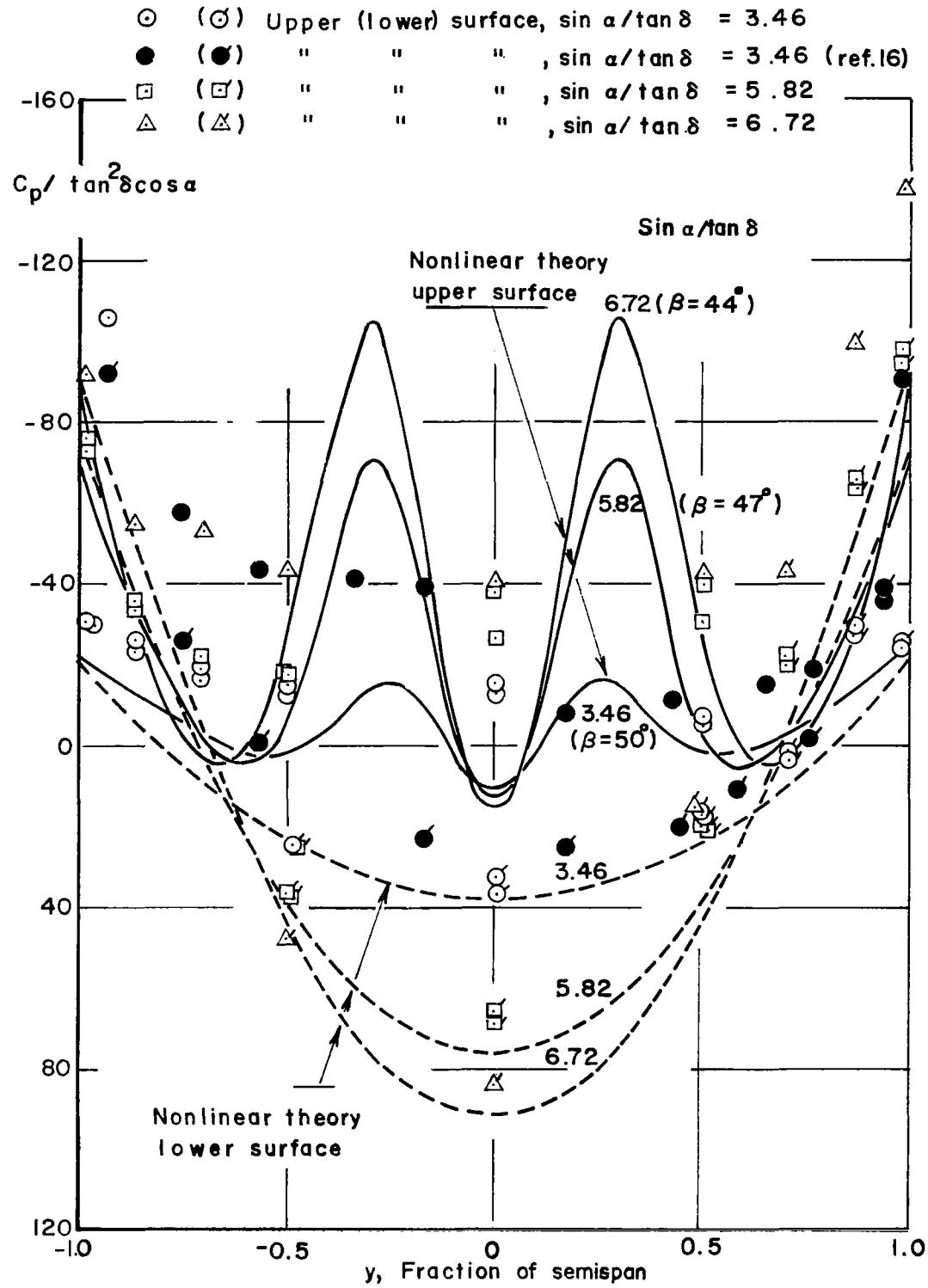

Figure 25. - Spanwise pressure distribution, circular cone without strakes.

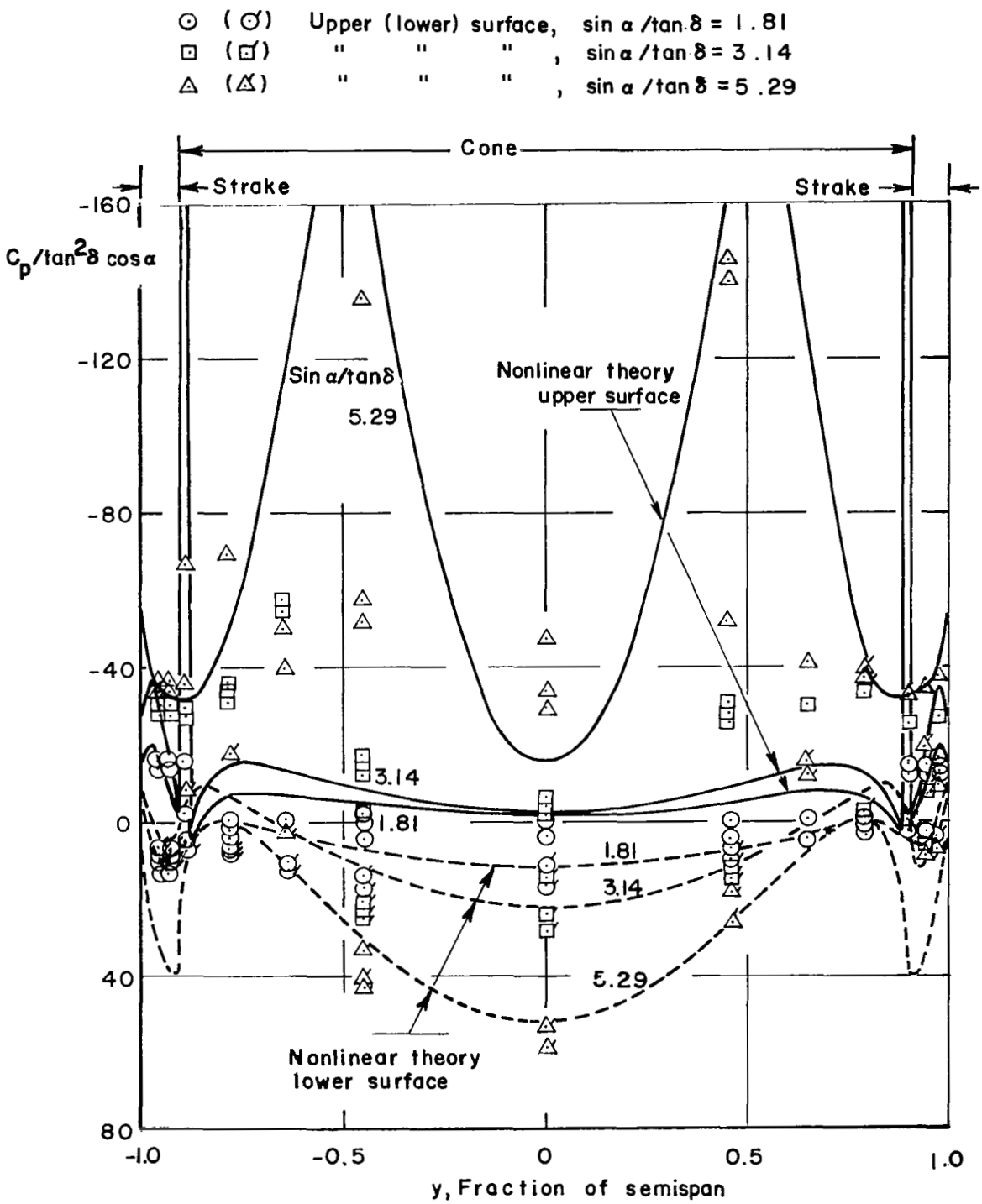

Figure 26. - Spanwise pressure distribution, circular cone with 10% strakes.

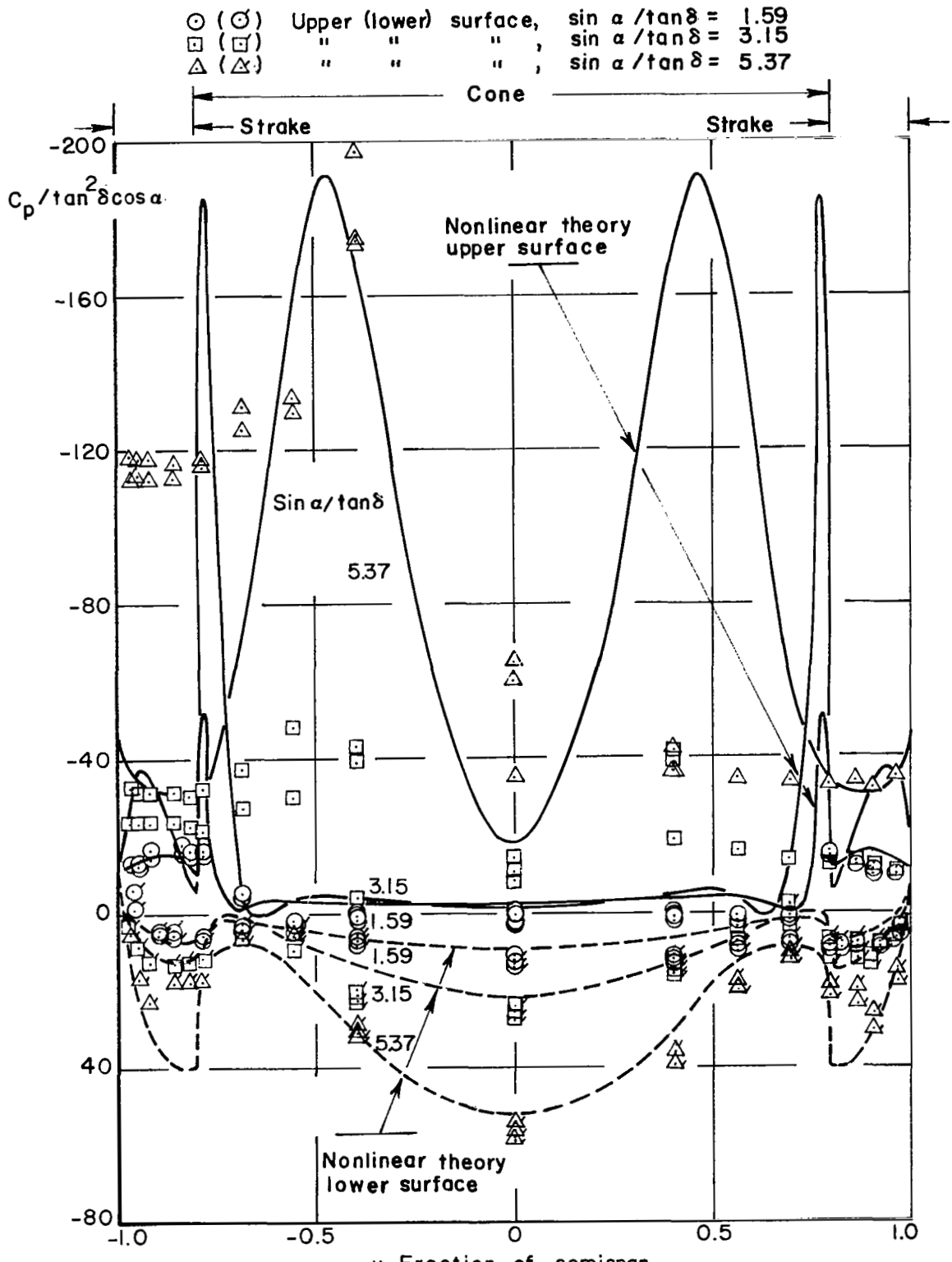

Figure 27. - Spanwise pressure distribution, circular cone with 25% strakes.

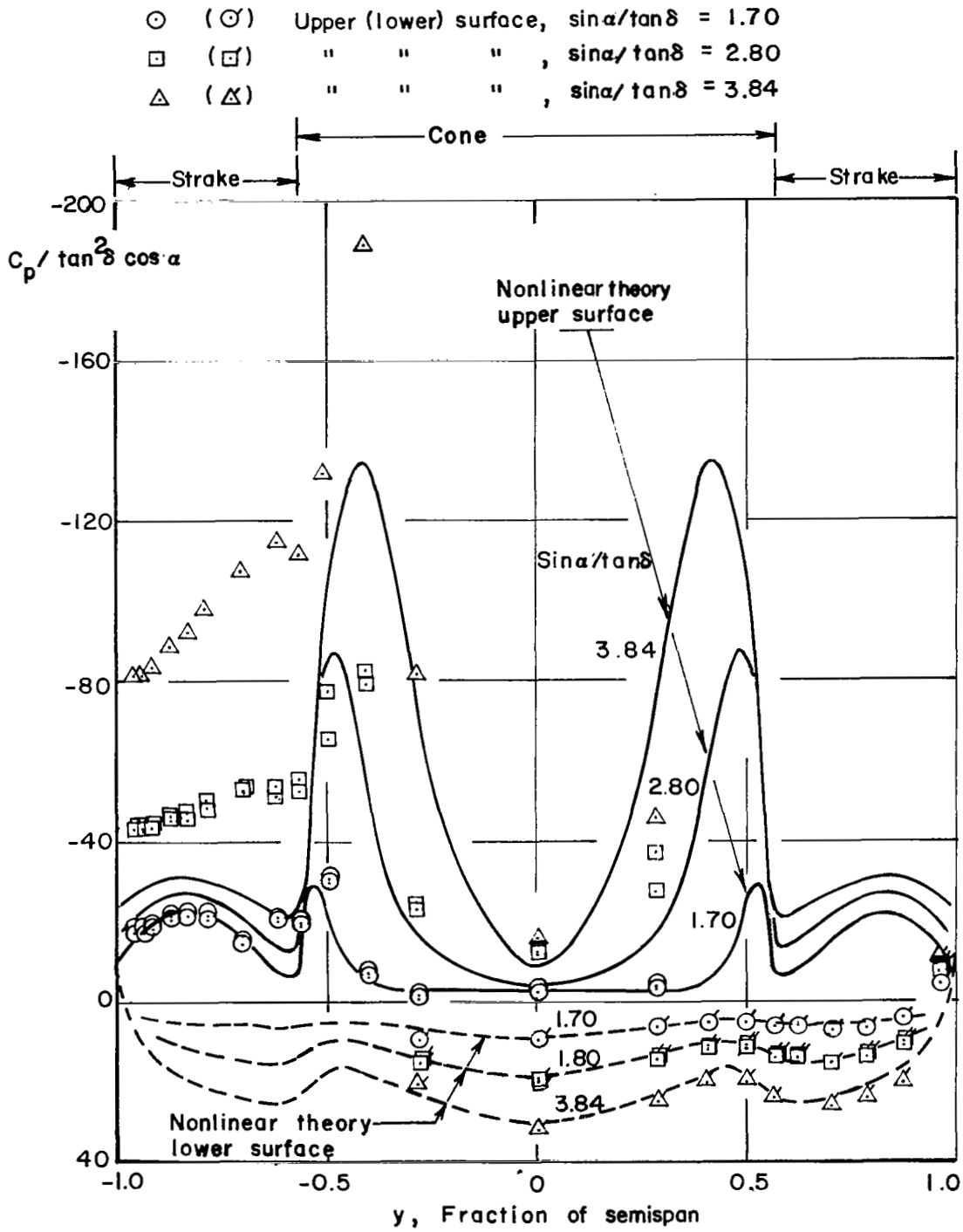

Figure 28. - Spanwise pressure distribution, circular cone with 75% strakes.